Scanning tunneling microscopy and spectroscopy study of the oxygen-induced effects on the Fe(001) surface and $3d$ metals/Fe(001) interface

January 19, 2012

Contents

Abstract

The uninterrupted efforts devoted over the last decades to continuously reduce the dimensions of devices have led to Nanotechnology, a discipline that aims to create and use structures, devices and systems in the size range of about 0.1 - 100 nm [1].

The two basic approaches to creating surface patterns and devices on substrates in a controlled and repeatable manner are the top-down and bottom-up techniques [2].

The top-down methods retain the lithographic design motifs by making use of tools such as nanolithographic techniques and scanning probe microscopies, imposing a structure or pattern on the substrate being processed. In contrast, bottom-up methods aim to guide the self-assembly of atomic and molecular constituents into organized surface structures through processes inherent in the manipulated system, with the aim to "engineer" electronic and magnetic materials on the atomic scale.

Common to all bottom-up strategies for the fabrication of nanostructures at surfaces is that they are essentially based on growth phenomena. In this respect understanding the processes of nucleation and growth on a substrate surface is of importance for growing high-quality nanostructures [3].

By tuning parameters like the substrate temperature and deposition rate one can change the kinetic conditions of growth and obtain structures that does not represent necessarily the minimum energy configuration of the system. The stabilization of this metastable structures is of particular interest in the case of magnetic materials, because they can have different magnetic properties depending on the morphological configuration.

Many of these features are related to the different mechanisms of strain relaxation in heteroepitaxial systems as well as to specific characteristics of atomic diffusion, such as the presence of Ehrlich - Schwoebel barriers hindering step crossings.

Some special growth techniques (use of surfactants and codeposition) can also be useful to overcome the elements natural limitations and produce accurately controlled, custom-designed epitaxial samples.

In this frame the preadsorption on the substrate of foreign atoms has been demonstrated to be effective in changing both the kinetics of growth and the minimum energy configuration of the system. In particular the presence of an ordered overlayer of oxygen on the Fe(001) surface affects the magnetic and electronic surface properties [4, 5]. Furthermore, it is well known that oxygen acts also as surfactant, promoting layer by layer growth whereas the

growth without oxygen is characterized by a roughness increasing with the coverage [6, 7].

In this thesis the atomistic processes involved in the oxygen mediated homoepitaxial and eteroepitaxial growth on Fe(001) surface will be discussed. In particular the oxygen induced effects on the Fe(001) surface and on the interface between the Fe(001) and two $3d$ metals, namely Cr and Ni are investigated.

In chapter 1 the properties of the oxygen passivated surface, the so called Fe(001)-$p(1 \times 1)$O will be exposed.

Chapter 2 is about the oxygen mediated growth of nickel and chromium ultrathin films on Fe(001).

In chapter 3 two different cobalt oxide nanostructure, the cobalt oxide thin films on Fe(001)-$p(1 \times 1)$O and cobalt oxide nanowire grown on Pd(1 1 19) vicinal surface are presented. The data about cobalt oxide nanowire grown on Pd(1 1 19) have been taken in collaboration with the group of the professor F.Netzer, during the period of six months I have spent at the Karl Franzens University of Graz.

Chapter 1

Oxygen induced effects on Fe(001) surface

1.1 Introduction

The interaction of oxygen with transition metal surfaces has long gained significant attention in both fundamental and applied research. Understanding the modifications in the crystallographic and electronic structure due to the presence of oxygen can improve the basic knowledge about fundamental processes such as oxidation, passivation, catalysis, and corrosion [8]. Furthermore, Fe-oxides are also of potential technological significance because of the magnetic properties of these systems.

In this chapter we will discuss the morphologic and electronic effects of the chemisorbed oxygen on Fe(001) surface. In particular we will focus on a particular phase, the so called Fe(001)-$p(1 \times 1)$O.

At a mesoscopic scale oxygen induces a strong step bunching and the oxidized surface is characterized by wide terraces separated by bunches of steps (Section 1.3).

At a microscopic level we found that the surface is covered by a perfect layer of chemisorbed oxygen and that the measured atomic corrugation is affected by the tunneling conditions used. The oxygen atoms are imaged alternatively as bright or dark spots depending on the tip-surface distance (Section 1.4).

The surface electronic properties of the Fe(001)-$p(1 \times 1)$O are shown in Section 1.5. The measured spectra provide information about the surface electronic density of states (DOS) and are interpreted with the aid of first-principles density-functional theory (DFT) calculations of the surface electronic structure. We show that our theoretical results are in good agreement

with Scanning Tunneling Spectroscopy (STS) experimental data, and permit to ascertain the spin character of the observed surface states at -0.5 and +0.9 eV. The theoretical calculations have been performed by the group of M.Trioni at the university of Milano Bicocca.

The oxygen surfactant properties during iron homoepitaxy are investigated from a microscopic point of view in Section 1.6. The oxygen overlayer is found to induce a layer by layer growth by lowering the interlayer mass transport barrier.

1.2 The Fe(001)-$p(1 \times 1)$O surface

Clean Fe(001) surfaces were obtained by ultrahigh vacuum (UHV) deposition of a thick Fe film (100 nm) on a MgO(001) substrate. All traces of contaminants (in particular oxygen and carbon) accumulated in the film during evaporation were removed by cycles of sputtering followed by flash annealing at 900 K for 1 min. Fe(001)-$p(1\times1)$O surfaces were realized by exposing a clean Fe(001) substrate held at 700 K to 30 langmuir (1L=1×10^{-6} $torr \times sec$) of pure O_2 (partial pressure: 4×10^{-7} mbar). The sample was then flash heated at 900 K for 1 min to remove the excess oxygen from the surface. The resulting surface is the oxygen passivated Fe(001)-$p(1 \times 1)$O, characterized by one oxygen atom per surface unit cell. Previous structural studies of the Fe(001)-$p(1 \times 1)$O surface have revealed that in this system the oxygen atoms are located in the fourfold symmetrical hollow sites of the surface, with the first Fe layer outward relaxed with respect to the bulk (see Fig. 1.1) [9, 10, 11, 12, 13]. Scanning Tunneling Microscopy (STM) images (see Fig. 1.2) show that this is a well ordered and defect free surface, with a perfect monolayer of oxygen covering the Fe(001) surface.

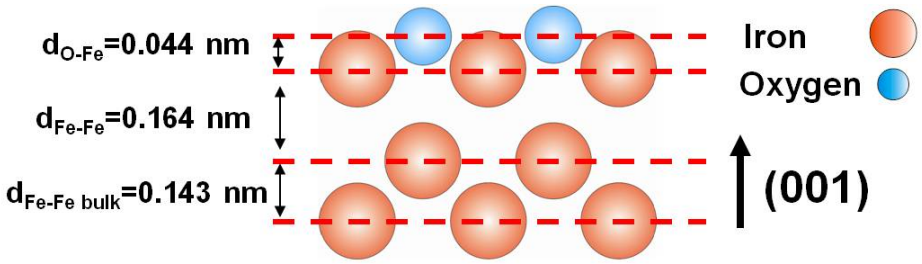

Figure 1.1: Side view of the Fe(001)-$p(1 \times 1)$O surface. There is an upward relaxation of the first layer.

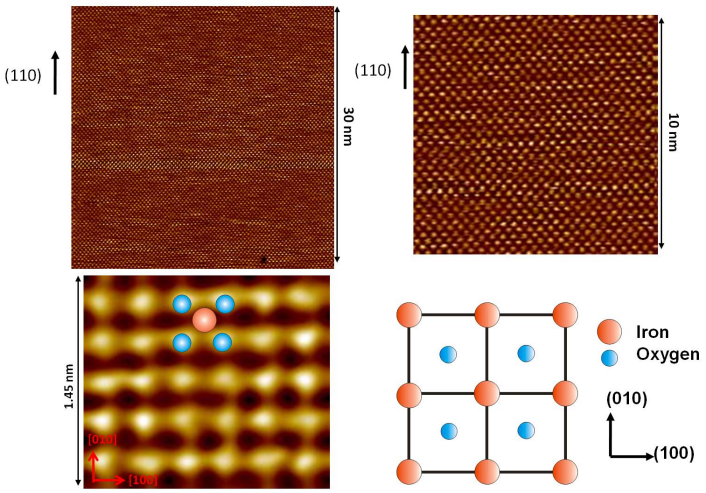

Figure 1.2: Atomic resolution of the Fe(001)-$p(1 \times 1)$O. The oxygen atoms are located in the fourfold symmetrical hollow sites of the Fe(001) surface

1.3 Terrace distribution

In this section we focus on the topographic changes occurring at a mesoscopic scale as a consequence of oxygen adsorption. The different morphology of the oxygen-free Fe(001) surface and of the Fe(001)-$p(1\times1)$O surface is shown in Fig. 1.3.

Note that both surfaces have been subjected to similar thermal treatments. The pristine Fe(001) surface is characterized by narrow terraces separated by monoatomic steps (height: 0.143 nm), while in the Fe(001)-$p(1\times1)$O surface several steps have coalesced, leading to steps several monolayers high. With respect to the oxygen-free Fe(001) surface, the step density is decreased and the surface topography is dominated by wider atomically flat terraces. In the oxygen-free Fe(001) surface, the steps between two terraces are all monoatomic. The terraces width distribution in the [100] direction is described by an asymmetric probability density function with an average value equal to 29.86 nm (standard deviation 35.43 nm). In the Fe(001)-$p(1 \times 1)$O surface only 5% of the steps are monoatomic. Their probability distribution is described by a symmetric bell-shaped function with an average step height equal to 4.71 atomic layers (standard deviation: 2.19 atomic layers). We have observed steps as high as ten atomic layers. The terrace width probability density in the [001] direction is also symmetric, with a mean value equal to 138.24 nm (standard deviation: 58.55 nm). The product between the step density and the mean step height is very similar (within 2%) before and after oxidation, thus we can deduce that the structure of the Fe(001)-$p(1 \times 1)$O

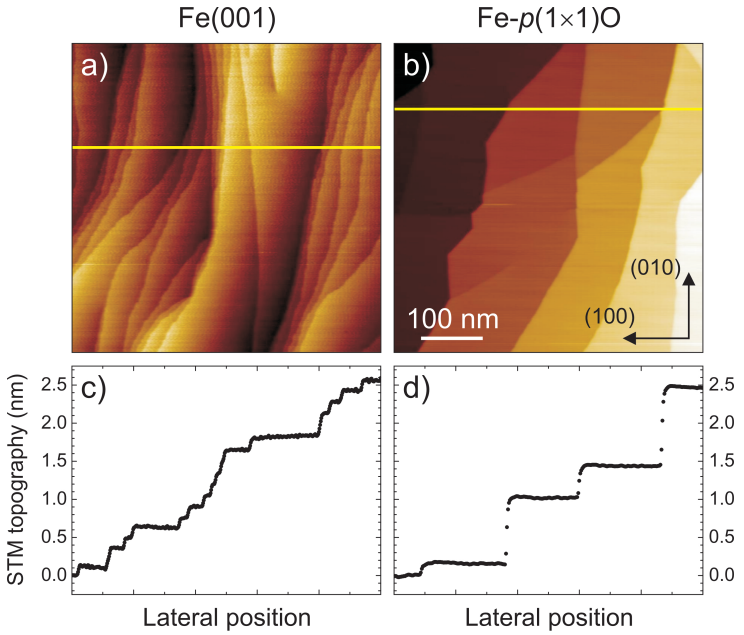

Figure 1.3: Terraced structure of Fe(001) and Fe(001)-$p(1 \times 1)$O. Image size is 500×500 nm^2. Panels (c) and (d) display the profile obtained along the horizontal lines in panels (a) and (b), respectively.

surface derives from the coalescence of the steps in the pristine Fe(001) surface. When the oxygen is removed from the Fe(001)-$p(1 \times 1)$O surface by sputtering and annealing, the starting morphology of the clean Fe(001) is recovered, and the steps are no longer bunched together. Apparently, step bunching (SB) is a direct consequence of the presence of chemisorbed oxygen. To address this phenomenon, we recall that many different mechanisms are known to produce SB on rough or vicinal surfaces [3]: (i) SB can be induced during growth and sublimation when a net flux of atoms attaches to or leaves from the terraces between steps [14, 15, 16](a mechanism also known as the Ehrlich-Schwoebel effect), or it might be caused by either (ii) electromigration [18] or (iii) elasticity [19, 20]. The second process can be ruled out in our case since no electric currents are forced across the sample, while the first one can be excluded since the preparation of the Fe(001)-$p(1 \times 1)$O surface does not involve a net mass flow landing or leaving the sample surface. In fact, no Fe is deposited and the amount of adsorbed oxygen exceeding one monolayer is removed by annealing at 900 K. The number of iron atoms that evaporate from the surface during the flash annealing is also negligible: at 900 K the iron vapor pressure is below 10^{-11} mbar. Note also that the final steps are straight, indicating a limited step meandering and excluding

the possibility that step bunching could occur by fluctuations of the step edges during annealing, leading to the occasional collapse of terraces. In this scenario Schwoebel has demonstrated that steps can move only in the presence of an effective long-range interaction between steps [15, 16]. This interaction is elastic in nature. Two steps separated by a terrace of width L experience a short-range repulsive force ("force dipole") and a long-range attractive force ("force monopole"), the latter existing only in the presence of strained layers. The repulsive force arises from an interaction energy of the form $\alpha_1 L^{-2}$ [100] between two adjacent steps, while the attractive one derives from an interaction energy of the form $\alpha_2 \log(L)$, where α_1 and α_2 are parameters that depend on the characteristics of the surface [21]. While it is generally accepted to model the repulsive strain field with a line of force dipoles along each step, there is no agreement in the literature about the magnitude of the dipole. The torque has been originally identified as the product of the surface stress with the step height but, according to Ibach, this model produces surface stress far too low (see,for example [23, 24]). On the other hand, α_2 is proportional to the magnitude of the overlayer strain, no matter whether tensile or compressive. As shown by Tersoff et al. combination of these two interactions can lead to a SB instability even in the absence of an external flux of atoms [22]. In this model the velocity of the steps is extremely sensitive to the temperature, so stress-driven SB should be a strong effect at high temperature, but it should be negligible at low temperature. In our case we observe that oxygen adsorption at room temperature does not change the step distribution, and step bunches develop only after the subsequent annealing. Therefore, the experimental evidence supports the idea that the SB observed on the Fe(001)-$p(1 \times 1)$O surface could be induced by the presence of an elastic attractive force between steps, possibly arising from the oxygen-induced stress. Generally, the intrinsic stress at a metal surface is tensile, due to a redistribution of the charge arising from the missing bonds above the surface atoms [23]. This charge unbalance causes two main effects: (i) the bonds between the first-layer and the second-layer atoms are strengthened, leading to a contraction of the spacing between the first and the second layer with respect to the bulk; (ii) electronic charge may accumulate among the surface atoms, giving a tensile stress. The chemisorption of foreign atoms saturates the surface atom bonds, removing in this way the charge between the surface atoms. This generally produces a reduction of the tensile stress. If the adsorbed atoms are electronegative with respect to the substrate they can even overcompensate the intrinsic tensile stress so that the resulting stress turns out to be compressive. A number of experimental and theoretical data confirm an oxygen-induced charge redistribution for adsorbed O on Fe(001) [9, 10, 11, 12, 13], due to the large electroneg-

ativity of oxygen compared to iron. Oxygen binds Fe with strong covalent bonds formed by Fe*3d-O2p* hybrid orbitals, similar to the ones in bulk FeO. The negative charge transfer from the substrate to the O adlayer is also confirmed by a 0.72 eV increase of the work function associated with an enhanced metal-surface dipole layer. The strength of the adsorbate substrate interaction gives a hint of the magnitude of adsorbed induced effects, therefore we expect that oxygen is likely to have a considerable influence on the stress of the outermost layers. In the pristine Fe(001) surface the distance between the first and the second layers is contracted by 3% with respect to the bulk spacing. This relaxation is reversed in the Fe(001)-$p(1 \times 1)$O surface, where the interspacing between the first and second layers is found to be larger than the bulk lattice parameter. Although there is no consensus concerning the amount of this relaxation, there is general agreement about the distance between the first and second layers in Fe(001)-$p(1 \times 1)$O being considerably larger than in bulk iron. First principles calculation performed by Chubb et al. shows a 23% increase [10], while Jona et al. inferred an expansion of 7% from low-energy electron diffraction (LEED) data [11]. More recently, Parhiar et al. determined an increase of 16% by combining x-ray diffraction and *ab initio* calculations [9].

In summary, both experimental and theoretical results confirm a picture in which the oxygen atoms in the Fe(001)-$p(1 \times 1)$O surface form with the first iron layer a strongly bound planar rocksalt FeO monolayer which is comparatively weakly bound to the Fe(001) surface. Since the O-Fe bond in the Fe(001)-$p(1 \times 1)$O is 4% shorter than the Fe-O bond found in bulk FeO, we can regard the surface as a single FeO strained layer placed on top of the Fe(001) substrate.

Another topic to be discussed is the influence of the repulsive force between neighboring adsorbate atoms in inducing a compressive stress. At low adsorbate coverage this direct repulsive interaction is negligible because the overlap between orbitals belonging to neighboring atoms decays exponentially. On the other hand, when the coverage is increased, this repulsion can become significant. In the Fe(001)-$p(1 \times 1)$O surface each Fe(001) hollow site is occupied by an oxygen atom, so one cannot exclude that the direct repulsion between oxygen atoms may play a significant role in determining the final surface stress.

As a conclusion of this section, we suggest that the observed oxygen-induced step bunching could derive from the attractive monopole force between the steps of a strained surface. In this frame, the role of oxygen is to greatly increase the absolute value of the stress compared with the Fe(001) surface. At the annealing temperature, because of the different strain, SB proceeds much faster in Fe(001)-$p(1 \times 1)$O than in Fe(001), determining the

different morphology observed in Fig. 1.3.

1.4 Atomic corrugation on Fe(001)-$p(1 \times 1)$O

When the oxygen is present as contamination on metallic surfaces, it appears generally as a depression in the STM images. This is true also for the oxygen contaminated Fe(001) surface [25]. In Fe(001)-$p(1 \times 1)$O, due to the (1x1) symmetry of the oxygen overlayer, it is not trivial to establish if the oxygen is imaged as a bright or dark spot. In particular, the tunneling conditions can influence the measured atomic corrugation.

In order to study a possible corrugation reversal as a function of the STM set points, it is essential to have a reference position, that can be located on a surface defect. The as grown Fe(001)-$p(1 \times 1)$O surface is usually very clean, flat on a scale of tens of nm and free of defects. It has thus been necessary to induce some kind of defects on the surface. This has been done by applying a short (few seconds) 1.5 kV Ar+ ion sputtering pulse. One can expect that a defect will consist of either a simple oxygen vacancy or a more complicated structure, resulting from a local redistribution of atoms.

In performing first-principles simulations, the Fe surface has been modeled by a slab composed of five Fe layers and O atoms adsorbed on both sides, in a periodically repeated supercell. Atomic coordinates of all atoms but the inner three Fe layers (fixed at the bulk spacing) have been obtained via optimization of the total energy of the system. All results have been obtained within the generalized gradient approximation for the exchange and correlation functional as proposed by Perdew, Burke, and Ernzerhof (GGA-PBE) [26], taking into account the spin polarization. The plane-wave ultrasoft pseudopotential method [27] lt was used as implemented in the PWSCF code of the Quantum-ESPRESSO distribution [28]. The pseudopotentials have been derived from scalar-relativistic all-electron atomic calculations. Fe and O pseudopotentials include *3d-4s* and *2s-2p* valence electrons, respectively. Nonlinear core corrections are used for Fe. The wave functions have been expanded up to a kinetic energy cutoff of 30 Ry; the effective potential and the charge density up to 200 Ry. The surface Brillouin zone integration has been performed with the Monkhorst-Pack scheme, adopting $k_{|}$|-point meshes equivalent to a 16x16 mesh in the irreducible surface unit cell of Fe(001). Constant current STM images have eventually been simulated by calculating the Kohn-Sham (KS) DOS in the energy interval between 1 eV below the Fermi level (E_F) and E_F, and by evaluating a constant density surface in the vacuum region [29, 30]. A Gaussian spatial broadening of 1 was finally applied to mimic finite experimental resolution. It must be noted

that this approximation does not consider the perturbation induced on the surface by the STM tip nor its spectral structure.

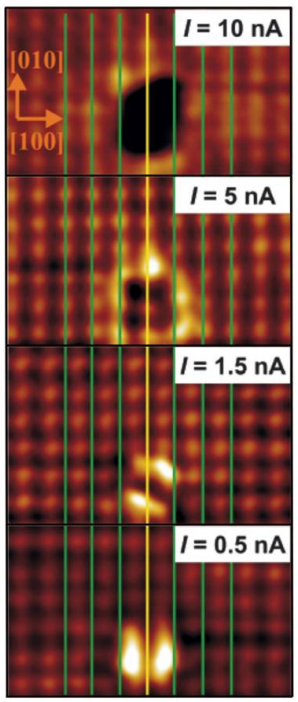

Figure 1.4: STM atomic resolution images of the Fe(001)-$p(1 \times 1)$O surface. The sample bias is set at V_b=0.1 V for every image, while the current set point is 0.5, 1.5, 5, and 10 nA, from the lower to the upper image, respectively. The image area is about 2.9x1.7 nm^2 for each image. The vertical lines are guides to the eyes for highlighting the corrugation reversal.

Fig. 1.4 reports atomic corrugation images of the Fe(001)-$p(1\times1)$O surface taken at a constant sample bias $V_b = 0.1$ V and at different current set points, with the tunneling current I equal to 0.5, 1.5, 5, and 10 nA, from the lower to the upper image, respectively. The tip-sample distance varies correspondingly, from larger to smaller values, with increasing current set points. We have estimated this distance as discussed in Ref. [31]: it results to vary from about 5 for I=10 nA to slightly less than 7 Å for I=0.5 nA. For each of the images reported in Fig. 1.4 we have drawn a horizontal line profile passing through the defect center the horizontal lines are not shown in Fig. 1.4. The profiles are collected in Fig. 1.5, where the center of the defect has been chosen as the origin of the horizontal position for each profile. By inspecting Fig. 1.5 as regards displacements larger than 2 unit cells from the defect center, one has an immediate evidence of an inversion between peaks,

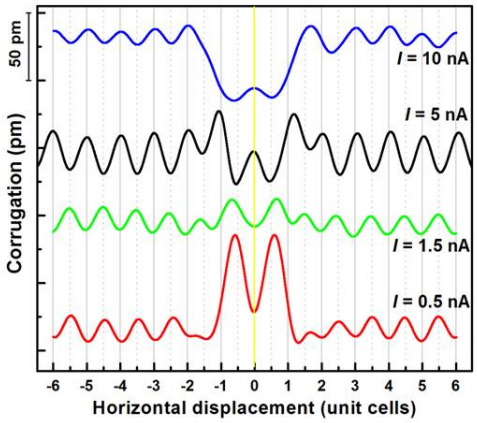

Figure 1.5: Horizontal line profiles of the STM images shown in Fig. 1.4. The lines pass through the center of the defect and are aligned making reference to such a feature central vertical line in Fig. 1.4. One unit cell is equal to 0.29 nm.

corresponding to protrusions in the images, and valleys, corresponding to depressions, when comparing the I=0.5 nA and I=1.5 nA with the I=5 nA and I=10 nA cases, respectively. Such an inversion can be evidenced also by inspecting the images reported in Fig. 1.4, which have all been aligned along the [010] direction, by keeping the center of the defect on the same vertical line. The vertical lines can help to observe that rows of protrusions in the two upper images I=5 nA and I=10 nA correspond to dim rows in the two lower images I=0.5 nA and I=1.5 nA. The known surface symmetry and unit cell eventually allow to identify this change in the atomic scale corrugation as either oxygen only or iron only atoms imaged in the two cases. This kind of corrugation reversal refers therefore to the distinct kind of atoms that are imaged by the STM with different experimental set points. A strong modification of the brightness levels is seen also on the defect itself (see below). We underline that the above results are not dependent on the bias condition, in particular on the sign of the tip-sample bias, provided its absolute value is small, typically below 100 meV. The use of larger biases generally resulted in less stable measurements with a worse resolution, so that they have not proved to be useful in determining the occurrence of a corrugation reversal.

A first, semi quantitative analysis of the corrugation reversal mechanism can be based on the observation that a charge transfer occurs between the surface Fe and O atoms, the latter being negatively charged. As a conse-

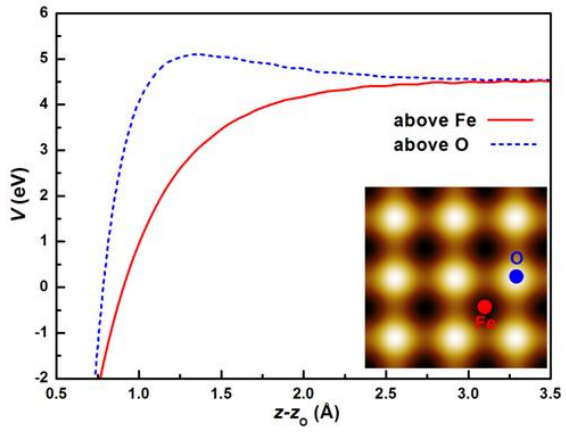

Figure 1.6: Electrostatic potential energy including ionic cores above the oxygen atoms (dashed blue line) and above the iron atoms (solid red line), along the (001) direction (z axis). Here, z_O represents the position of the oxygen atoms on the z axis. Inset: simulated STM image for the Fe(001)-$p(1 \times 1)$O surface at an average distance z=2 Å

quence, the electrostatic potential acting on the electrons outside the surface is lower on top of Fe than on top of O atoms (solid and dashed lines in Fig. 1.6, respectively). We remark that such a potential has been evaluated by considering the actual optimized positions of both O and Fe atoms at the surface. The difference in the potential suggests that the electronic wave functions decay in the vacuum (z direction) more slowly when moving outward above the position of the iron atoms, compared to moving above the position of the oxygen atoms (see the reference spots in the inset of Fig. 1.6), therefore leading to the reversed corrugation at large distances. This qualitative and physically sound explanation is however not fully reproduced by our analysis based on DFT (see below).

Numerical simulations of the STM images have been performed at an average distance from the oxygen layer of about 2 Å. The use of either positive or negative small biases provided qualitatively identical images. The results are equivalent to those obtained in our previous investigation and are shown in the inset of Fig. 1.6).

At this distance the geometric contribution prevails and the bright spots correspond to the protruding oxygen atoms. This result should be compared with experimental data measured at high currents, hence sampling the surface at short distances. To simulate the image at larger distances, an increased computational effort would be required (mainly, a larger basis set

and a thicker slab). In principle, aiming to obtain the greatest deal of information from theoretical computations, this could still be afforded thanks to the small unit cell of the $p(1 \times 1)$ structure. On the other hand, the reliability of simulated images in such situations is limited by the fact that the exchange-correlation contribution to the total KS potential has been approximated by GGA, which is unsuited to capture the proper long-distance behavior. The corresponding results are reported here for the sake of completeness only: we could span a distance range up to 8 Å, where the electron density of states is 109 times smaller than the maximum value in the cell, and found that the simulated corrugation monotonically goes to zero with increasing distance, without ever reverting.

Finally, it is worth reminding that we do not consider the effects of the tip in the image formation. Nevertheless, we emphasize that the series of images shown in Fig. 1.4 could be repeatedly obtained, without significant modifications, by increasing or decreasing the tip-sample distance across the two atomic corrugation regimes. We can thus exclude that the corrugation reversal is due to a sudden irreversible alteration of the tip.

We take now a closer look at the defect chosen as a reference for the investigation of the corrugation reversal, with the aim of understanding if our experimental and theoretical approaches allow to infer its nature. The topographic characteristics of this defect are best appreciated in the image taken at V_b=0.1 V and I=5 nA. On account of the previous analysis, we assume to be close enough to the surface to have the geometrical contributions dominating over the electronic ones in determining the topographic image of the surface, as seen by STM. Therefore, the protrusions seen on the image, excluding the defect region, are assigned to oxygen atoms. In order to simulate the defective surface, we make the assumption that the defect consists of an oxygen vacancy.

This choice is supported by an inspection of Fig. 1.7, which shows a blow up of the defect site and of its first neighbors, and by considering the surface preparation conditions mentioned above and the short tip-sample distance (high tunneling current regime). The defect, in particular, is centered on an oxygen site, involves a limited region, and presents a fourfold symmetry. Moreover we observe, by comparing different images of the same defect taken in the high current set point regime, and always making reference to the center of the defect, that both the first- and the second-neighbor protrusions are brighter than all of the other protrusions seen in the image. In the simulation we have thus removed an oxygen atom from the perfect p(1x1) surface, on both sides of the slab, and relaxed the structure in a (4x4) surface unit cell. Upon removal of the central oxygen atom, the four first-neighbors oxygen atoms relax in-plane toward the vacancy by 0.14 Å, with a negligible vertical

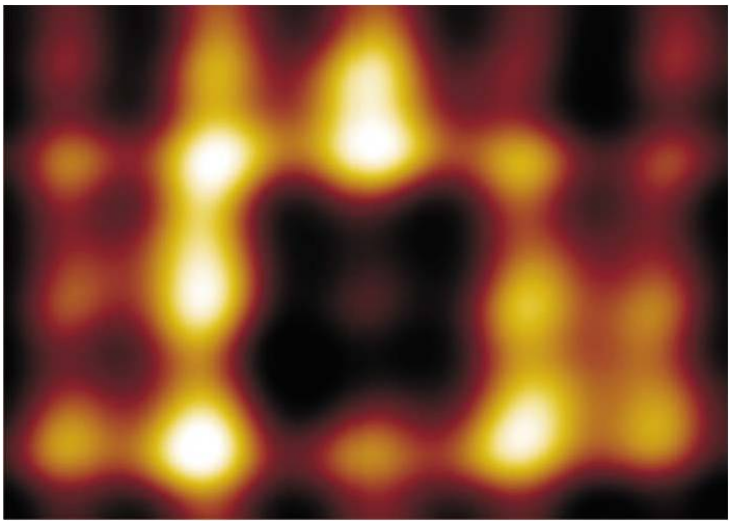

Figure 1.7: Blow up of the defect seen in the STM image of Fig. 1.4 with set point $V_b = 0.1$ V and I=5 nA. The image area is about 1.5x1.2 nm^2.

displacement. The in-plane relaxation of the four in-plane first-neighbors Fe atoms amounts to 0.05 Å toward the vacancy and 0.06 Å in the vertical direction, reducing the separation from the inner Fe layer. The total energy of this relaxed surface is 0.26 eV lower with respect to the unrelaxed one. A snapshot of the geometric configuration is reported in Fig. 1.8.

Using this configuration we computed the STM image; the result is reported in Fig. 1.9.

The average distance between the chosen isosurface and the oxygen layer is about 2 Å. This distance must be related to a measure obtained in a high current regime, as that reported in Fig. 1.6. The main feature of the experimental results, i.e., the increased brightness of the O atoms close to the vacancy, is indeed nicely reproduced. It is worth to notice that, in the central region, the absence of the oxygen atom should require a shorter tip-surface distance to keep a fixed current. Possibly, the weak bright spot at the center of the defect shown in Fig. 1.7, which is missing in the simulated image shown in Fig. 1.9, could be due to the influence of the scanning tip. The overall good agreement between the two set of results suggests to actually identify the measured defect as due to an oxygen vacancy.

On the basis of the experimental and theoretical results described in the previous sections, we now consider and discuss three main factors that can be taken into account to understand how the STM images of both the perfect and the defective Fe(001)-$p(1 \times 1)$O surface take shape. The first and more intuitive factor is the geometrical configuration, which is often invoked to

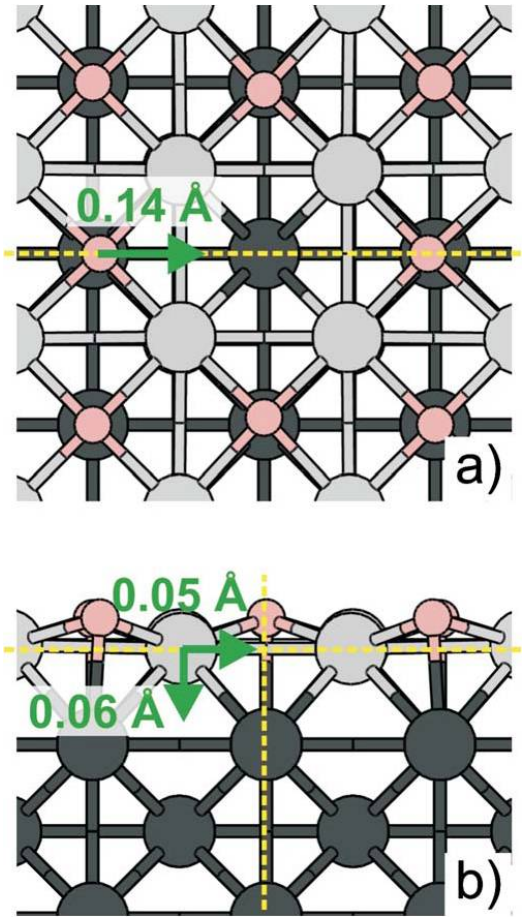

Figure 1.8: (a) Top view and (b) side view of the relaxed defective surface. The small circles represent the O atoms; the large circles represent the Fe atoms, both in the first layer (light gray) and in the layers below (dark gray). The arrows indicate the atom displacement, along the directions of the dashed lines, upon relaxation (see text).

identify the brightest spots with the atoms located in the highest position with respect to the surface. In the present system, however, the presence of two atomic species suggests that this direct interpretation can easily be misleading. Moreover we have seen, when analyzing an oxygen vacancy, that the O atoms close to the defect, which experimentally appear to be brighter than the others in the image, are actually at the same distance from the surface as any of the others. We must therefore exclude that the geometrical arrangement of the oxygen atoms can be considered as the main reason for the experimental evidences. A second contribution to be reckoned in is the charge distribution (or, more precisely, the local density of states in the proper

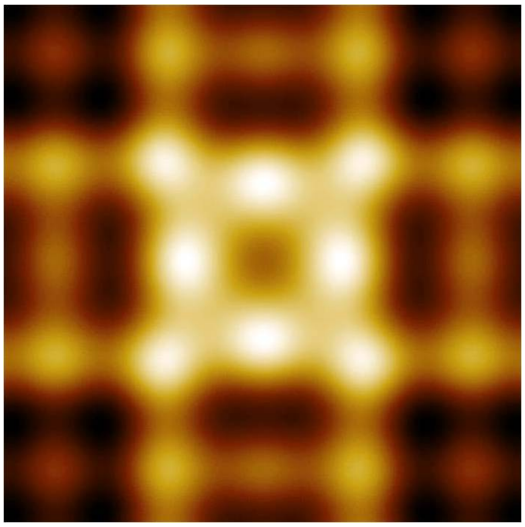

Figure 1.9: Simulated STM image for the relaxed defective surface.

energy interval close to E_F) on the different atoms present at the surface. By performing a Lwdin charge analysis [32], we find that in the perfect Fe(001)-$p(1 \times 1)$O surface each oxygen atom holds an additional electron captured from the underlying Fe atoms. Upon removal of an oxygen atom, such an electron is shared between the five first neighbors Fe atoms (four in the surface plane and one in the first layer below) and only a small fraction of the charge is distributed on the other O atoms. Moreover, we do not find significant differences in the local density of states at the atoms nearest to the vacancy, when compared to those on the perfect Fe(001)-$p(1 \times 1)$O surface. We conclude that the details of the charge distribution on the specific orbitals of the different species present at the surface, even if possibly modified upon the defect creation, have a negligible influence on the details of the image formation of the oxygen vacancy. Finally, we discuss the role played by the decaying behavior toward the vacuum of the electronic wave functions involved, which is affected by the local potential barrier above the surface. A modification of such a barrier, caused either by oxygen adsorption, when passing from the pristine Fe(001) surface to the Fe(001)-$p(1 \times 1)$O surface, or by oxygen removal, when the vacancy is created, can in fact be responsible of either promoting or hindering the tunneling process to the STM tip. The contribution of the local potential barrier remains the only one that can play a role in the corrugation reversal previously discussed for the Fe(001)-$p(1 \times 1)$O surface. We remark that possible alterations of the surface potential barrier might in principle be induced also by the interaction with the STM tip, whose effect has not been considered in our analysis. Nevertheless we note

that, to explain the observed findings, such tip induced alterations should be more effective when the tip is farther from the surface than when it is closer, which seems a counterintuitive result. It is therefore interesting to evaluate the variation of the potential acting on the electrons due to the creation of the O vacancy. To this purpose, we report in Fig. 1.10 the difference in the KS potential between the defective surface and the one obtained by reintroducing the removed O atom into the vacancy site.

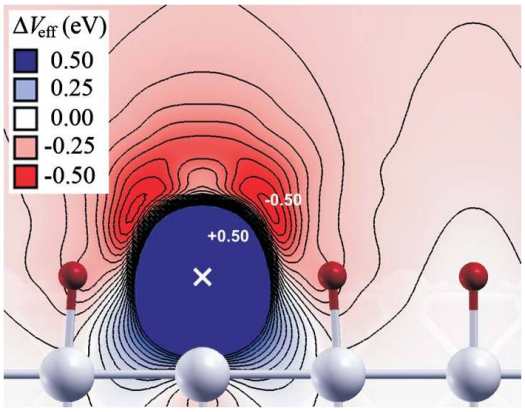

Figure 1.10: Difference in the effective KS potential between the Fe(001)-$p(1\times1)$O surface with the vacancy (i.e., in absence of the O potential, which is strongly negative close to the nucleus) and the same surface without the vacancy (indicated by a white cross). The small spheres represent the O atoms; the large spheres represent the Fe atoms in the first subsurface layer.

The dark shaded region (blue in the color version), $V_{eff} = +0.5eV$) around the vacancy site (i.e., in a region around the defect position of smaller extent than the atomic size) corresponds to an increase of the potential in presence of the vacancy, mostly due to the missing potential of the removed O atom, which is strongly negative close to the nucleus. On the contrary, in the less dark (red in the color version,) $V_{eff} = -0.5$ eV) symmetric lobes above the vacancy region the potential is lower and consequently the decay of the wave functions is slower. To be more intuitive, the latter regions represent preferential channels for the tunneling process. Thanks to the presence of these channels, the electron states on the O atoms closest to the vacancy can more easily extend away from the surface, therefore resulting in the increased brightness of the first neighbor O atoms. On the other hand, in the vacancy position, the STM tip would be forced to come closer to the surface to succeed in coupling its electron states with those of the sample, there mainly located in the subsurface Fe atom.

As a final remark, we underline that one should not deduce, from the

previous considerations, that the atomic configuration is irrelevant in determining the STM image formation, even though no significant O vertical displacements are found upon the relaxation following the creation of the O vacancy. In fact we have verified, by further simulations, that the STM image obtained with an unrelaxed atomic configuration (not shown here) is much different from the one shown in Fig. 1.9. Such an image actually shows a very pronounced bright spot on top of the vacancy, which overwhelms the other features, and does not reproduce the experimental evidence.

In conclusion, in this section we have focused our attention on a corrugation reversal between oxygen only and iron only atoms seen on the Fe(001)-$p(1 \times 1)$O surface, as a function of the tip-sample distance. Comparison between experimental images and first-principles calculations suggests that the observed phenomenology is due to the different local potential barrier on top of either O or Fe surface atoms. Based on this conclusion, we have analyzed an oxygen vacancy created on the surface, and have been able to produce a simulated image in fairly good agreement with the measurements. We believe that our study can represent a suitable general approach for the interpretation of STM images of oxidized metal surfaces where, in particular, the geometrical structure cannot be a support for the understanding of the experimental observations.

1.5 Electronic structure

The STM/STS measurements have been performed using an Omicron Variable Temperature (VT)-STM in a UHV chamber connected to the preparation system. STS spectra (i.e., dI/dV curves) for the investigation of the sample DOS have been acquired at room temperature, using a lock-in amplifier with a modulation amplitude of 50 mV. In order to increase the signal-to-noise ratio, all the presented STS spectra are the result of an average over tens of acquisitions at same sample-tip bias V_b (sample bias with respect to the tip) and tunneling current I_t set point, i.e., at the same tip-sample distance. First principles calculations of the surface electronic structure are performed within the DFT, using the generalized gradient approximation (GGA) for the exchange and correlation energy functional. We use the embedding code implemented by Ishida [33] to treat realistic surfaces through all-electron full-potential calculations. This Green function based embedding scheme [34] is able to consider a system which is infinite, periodic in the surface plane but nonperiodic along the surface-normal direction z. A finite embedded region along z is defined requiring that the perturbation due to the surface is well screened inside. The problem is then solved in such a

region only. For the clean ferromagnetic iron surface we have verified that the perturbation is quite well screened within four layers beyond the surface. In addition, also the oxygen overlayer and 11 Å of vacuum have been included in the embedded region. Generalized boundary conditions guarantee the correct behavior of the solution at both the bulk and the vacuum side. The Greens function was expanded on a linearized augmented plane waves (LAPWs) basis set using 11.6 Ry as cutoff. We set l_{max}=9 for the maximum angular-momentum number of the spherical expansion inside the muffin-tins, whose radii are 1.2 and 0.85 Å for iron and oxygen, respectively. The relaxed surface atomic geometry has been taken as reported in Ref. [10]. The surface Brillouin zone (SBZ) was sampled by a 18x18 regular mesh which was reduced to a set of 55 indipendent $k_{||}$ points.

STS data have been acquired both on the clean and on the Fe(001)-$p(1\times1)$O surface. We observe that the spectral features that can be extracted from our measurements are independent of the lateral position of the tip with respect to the surface unit cell and consequently can be considered as average properties of the whole surface. Prior to the analysis of the Fe(001)-$p(1\times1)$O surface, we performed an STS investigation of clean Fe(001) in order to check the surface quality before oxidation. A peak at about +0.2 eV was observed in normalized dI/dV curves, in agreement with previous measurements [35] and with our simulation (not shown). Raw dI/dV experimental data from the Fe(001)-$p(1\times1)$O surface (inset of Fig. 1.11) show two features at roughly 1 eV above E_F and 0.5 eV below E_F. In order to perform a detailed analysis of the surface DOS features, thus allowing a direct comparison with *ab initio* simulations, STS curves have been analyzed using normalization to the tunneling barrier transmission coefficient T [36], instead that to the experimental total conductivity I/V [37]. In the framework of a onedimensional (1D)-Wentzel-Kramers-Brillouin (WKB) treatment of the tunneling current, it is possible to show that the following approximated expression holds:

$$\rho_t(0)\rho_s(eV) \propto \frac{dI/dV}{T_s} \,, \tag{1.1}$$

formula where s is the sample electron DOS at energy eV with respect to E_F, t_0 is the tip electron DOS at E_F; V is the sample bias; $T_s = A[T(eV), V, z) + T(0, V, z)$ is a symmetrical combination of the barrier transmission coefficient $T(\varepsilon, V, z)$. Using a 1D-WKB rectangular approximation, T can be written as

$$T(\varepsilon, V, z) = exp[-2z\sqrt{\frac{2m}{\hbar^2}(\phi + \frac{eV}{2} - \varepsilon)}] \tag{1.2}$$

where z is the tip-sample distance and ε the effective work function. It

can be shown that using a normalized dI/dV the sample DOS is probed mainly at positive applied voltage (unoccupied states), while the tip DOS is probed mainly at negative bias [36]. However, assuming that the tip DOS is nearly constant in the measured region, and higher than sample DOS at Fermi level, Eq. (1.1) gives information about both occupied and unoccupied DOS in the surface region, provided the negative bias is not too large, i.e., it can be employed to extract also features related to sample occupied states [38]. Reliable effective values of work function and tip sample distance are required to perform this normalization. As discussed in [38], there are different possibilities to evaluate these parameters from STS data. Here we estimate the tip-sample distance by fitting the exponential tails of the dI/dV spectrum and assuming an effective work function of 4.5 eV; however, the choice of the work function does not influence the results and the discussion reported below. The tip-sample distance obtained with the fitting procedure, thus, represents an effective value to be used for the recovery of the sample DOS within a 1D description of the tunneling process and provides a rough but reasonable estimate of the real tip-sample distance.

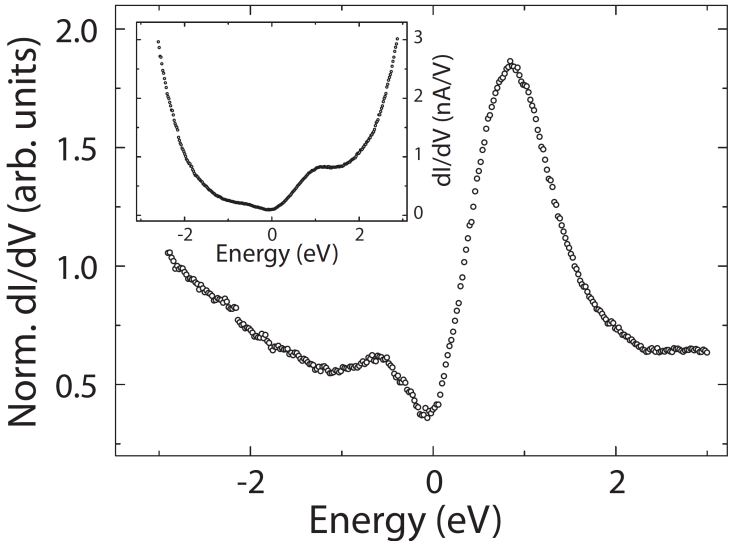

Figure 1.11: Normalized STS spectrum of the Fe(001)-$p(1 \times 1)$O surface (measurement set-point: current $I_t = 0.4$ nA, bias $V_b = 1$ V). Inset: raw dI/dV experimental data.

A normalized dI/dV curve of the Fe(001)-$p(1 \times 1)$O surface is shown in Fig. 1.11. This spectrum has been measured imposing a low set-point tunneling current I_t(0.4 nA, corresponding to a relatively large tip-sample distance), so that the perturbation induced by the tip is minimized. From

the normalization procedure explained above we can estimate a tip-sample distance of about 8 Å. Two features are detected at about +0.9 and -0.5 eV. These features are always observed using different W tips and have also been measured using bulk Cr tips [39]; we can thus safely attribute them to the sample electronic structure. In order to interpret the measured STS spectrum we studied the Fe(001)-$p(1\times1)$O surface from first principles. The number of theoretical studies is scarce; the main part of them is devoted to the structural properties of the system [10, 12, 13] and only few works discuss spectral properties [40, 41]. One of the most accurate calculation has been performed by Clarke et al. [42] and it shows the surface band structure along a high symmetry path of the SBZ. In their work surface states are distinguishable from the discrete features that form the projected bulk bands, on the basis of the spatial localization of the wave function in the surface region. In our embedding approach, due to the infinite extension of the substrate, the surface band structure is a continuous function of the energy for each k point of the SBZ so that surface resonances and discrete states can be easily evidenced. The adsorption of oxygen on the iron surface leads to a partial modification of the surface electronic properties. Although the bonding p levels of oxygen lie very deep in energy, the antibonding states, which extend for some eV around the Fermi level, hybridize with the Fe surface atoms electronic structure. In Fig. 1.12 we report the computed surface band structure for the majority (left panel) and the minority (right panel) spin components calculated in the first Fe and O layers. The brighter regions correspond to higher density of states and narrow lines are very sharp features. The less dispersive d bands extend in the energy interval between -5 and -1 eV for the majority component and between -2 and 2 eV for the minority one. We note that due to the surface band narrowing the exchange splitting at the Fermi level is larger than in the bulk. Surface states can be identified as the brightest lines in Fig. 1.12. In particular at majority-spin surface states are found at -3, -1.6, and -0.8 eV. On the other hand minority spin surface features lie at higher energies, namely at -0.35 eV, in a 1 eV wide range above the Fermi level, at 1.7, and 2.1 eV.

In Fig. 1.13 we report the computed density of states evaluated in the two surface layers (Fe and O), in the energy interval proper of the STS measurements. The majority and minority components are reported in the upper and lower panels, respectively, while the dotted line corresponds to the total DOS.

No evidence of adsorption induced surface-state reorganization with respect to clean Fe(001) is found in the majority component. On the other hand the minority-spin feature (found at 0.18 eV) of clean Fe(001) is not observed upon adsorption of oxygen, while a peak at 0.8 eV is found that

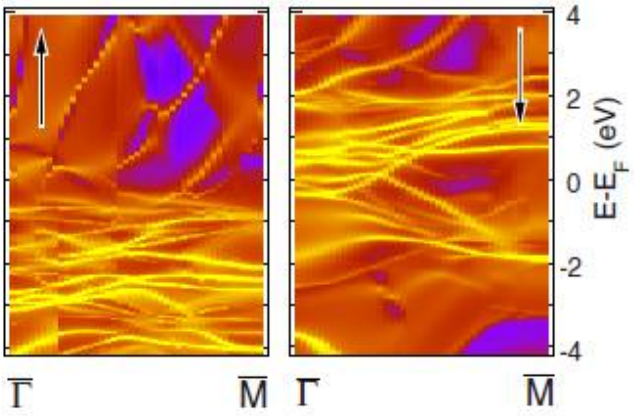

Figure 1.12: (a) Computed density of states of Fe(001)-$p(1 \times 1)$O in the surface region (surface and subsurface layer). (b) Computed density of states of Fe(001)-$p(1 \times 1)$O integrated only into 1/5 of the SBZ around ; upwards arrow: majority-spin component; downwards arrow: minority-spin component; dotted line: total DOS.

we identify as a surface resonance due to its large amplitude in the vacuum region. We observe that the computed position of this unoccupied minority surface state is in very good agreement with the measured position of the large peak at positive bias in STS data. A further effect of the O-Fe interaction is represented by the enhancement of the magnetization in the surface iron layer (passing from 2.97 μ_B of the clean surface to 3.22 μ_B upon the oxygen adsorption) and the appearance of a spin polarization also in the oxygen layer, which we calculated to be equal to 0.22 μ_B, in agreement with previous findings [40, 10]. Due to the faster decay toward the vacuum of the wave functions at large k, the STS probing method has a higher sensitivity to states around the Γ point. This is usually the case for surface states, even though different situations can exist, since the decay in vacuum depends on the specific dispersion relation for the considered surface state. This aspect is not considered in the 1D-WKB normalization procedure of experimental data. A simple method in order to permit a qualitative but direct comparison between measured STS data and theoretical DOS, which would not be otherwise straightforward, is to integrate the latter one in a smaller region of the SBZ [35]. Here, considering the contribution to the DOS only from 1/5 of the SBZ around Γ, we obtain some new features with respect to the total DOS, which give account of the measured peaks. In addition to the main minority peak at +0.8 eV, structures at the Fermi level in the minority component, peaked at about -0.35 eV, appear, together with a structure at

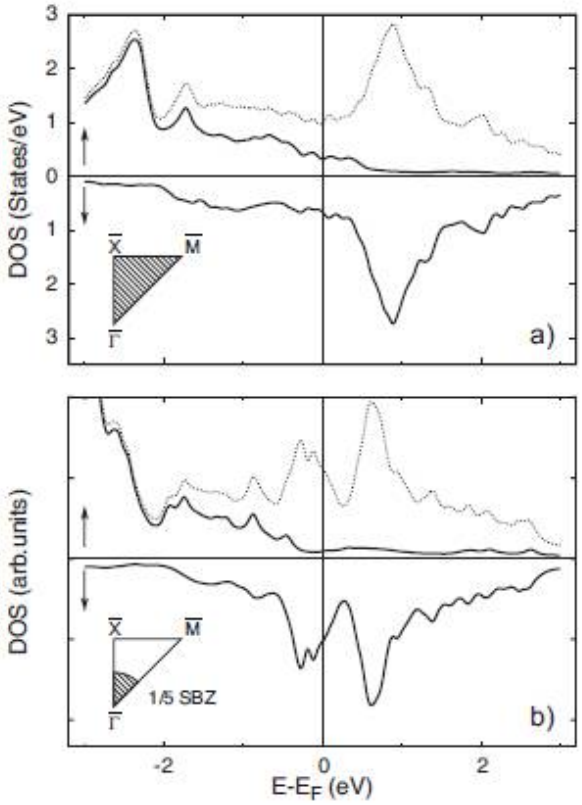

Figure 1.13: Computed surface band structure of Fe(001)-$p(1\times1)$O: majority and minority-spin components are reported in the left and right panels, respectively.

-0.9 eV in the majority component (see Fig. 1.13b). The enhancement of the spectral weight of these structures upon integrating within a restricted region of the SBZ is due to the flat dispersion around the Γ point. In this way satisfactory agreement between experiment and theory is obtained not only for the minority peak at +0.8 eV, but also for the structure at negative energy (-0.35 eV from theory vs -0.5 eV from experiments). The agreement is even better if effects related to measurement conditions are taken into account. *Ab initio* calculations indicate the minority-spin character of the measured surface states. We observe that the broadening of the measured features with respect to calculations could be related to a convolution of the fine structures visible in Fig. 1.13.

Now we discuss the influence of measurement conditions. We have already mentioned that minimizing the tunneling current and the tip electric field (i.e., at large tip-sample distance) corresponds to a situation which is closer to the unperturbed isolated surface (in equilibrium). When a larger set-point

tunneling current is employed for STS measurements, the corresponding tip-sample distance is decreased, leading to a significant perturbation of the system, a shift of the above discussed peaks is observed. In Fig. 1.13 we show normalized dI/dV data from the Fe(001)-$p(1 \times 1)$O, acquired using different ($I_t V_{,b}$) set points (in particular different set-point current in the range from 0.4 to 5.3 nA, keeping the set-point bias at 1 V). The same two

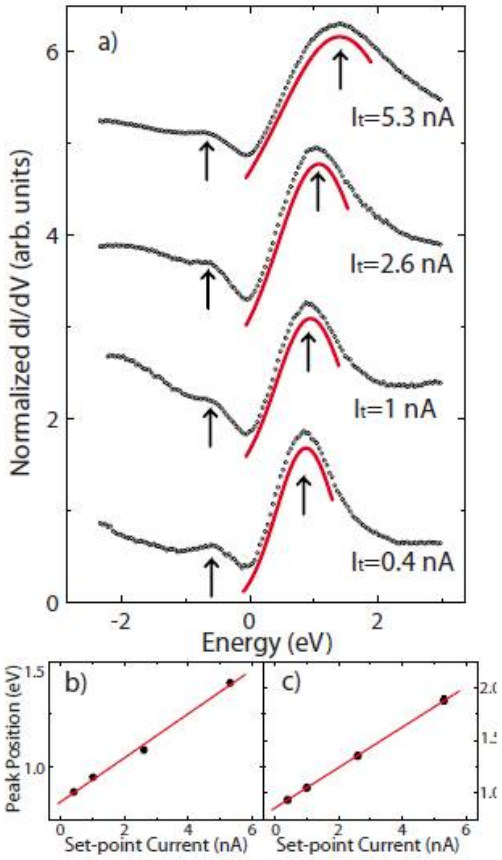

Figure 1.14: (a) Normalized STS spectra of the Fe(001)-p(1x1)O surface, measured at different values of the setpoint current I_t (V_b=1 V). The arrows indicate the energy positions of the surface states; Gaussian fit for the feature in unoccupied states is shown (solid line). (b) Position and (c) width of the peak in the unoccupied states as a function of set-point current I_t. Linear fit is shown (solid line).

features commented above are detected; nevertheless both peaks broaden and shift away from the Fermi level when increasing the tunneling current I_t. This observation is not affected by the normalization procedure, i.e., the same trend as a function of set-point can be detected in raw (i.e., non-

normalized) dI/dV data (not shown). In order to quantitatively evaluate these effects, we performed a Gaussian fit of the large feature. Both position and width increase linearly when increasing it, as shown in Fig. 1.14. From the linear fit, we can extrapolate the peak position E_0 and the full width at half maximum (FWHM) w_0 at zero current, and we obtain E_0=0.83 eV and w_0=0.85 eV respectively. A similar effect (shift to more negative bias) is qualitatively observed for the peak in the occupied states, even though much less marked (and difficult to quantify, since the feature is weak and not easily separable from the background). We note that this kind of effect is not observed on the clean Fe(001) surface,i.e., the position of the peak at +0.2 V is not influenced by the tunneling current. Also, the large shift detected when the set-point current increases from 2.6 to 5.3 nA corresponds to a very small difference in tip-sample distance (a reasonable estimate provides $\Delta z < 0.5\mathring{A}$). Different effects have been invoked in the literature to explain observed shifts of STS features as a function of the measurement set point, i.e., of the applied electric field between tip and sample and/or of the tunneling current, for instance tip-induced band bending (in semiconducting surfaces) [43], Stark effect [44], different decay behavior of surface wave functions into vacuum,[45] and transport-limited surface charging (i.e., setup of a nonequilibrium surface configuration, in which one or more electrons are injected into unoccupied surface states) [46]. Even though no definite conclusion can be drawn in our case yet, simple arguments indicate that some of these effects can be ruled out. In fact, band bending effects are typical of semiconductors, being electric field effects in metal surfaces usually much smaller. Also, the large shift detected upon a small change in tip-sample distance (i.e., going from 2.6 to 5.3 nA set-point current) points into the direction of excluding effects related to the tip electric field perturbing the system, or to the different decay behavior of surface wave functions into vacuum. Within this simple scheme, an out-of-equilibrium configuration due to electron injection in the surface seems to be the major responsible for the observed shift. In this context, we note that the situation for STS is qualitatively similar to inverse photoemission spectroscopy (IPS), in which electrons are also added to the system. In particular, IPS data from Fe(001)-$p(1 \times 1)$O identify a surface feature (located at 1.8 eV above E_F) that is shifted to larger energy with respect to theoretical expectations [47]. In that case, the discrepancy has been attributed to the difference between the excited states in the presence of an extra electron (sampled in IPS) as compared to those calculated for the unperturbed system. This difference can originate sizable shifts of the spectral features toward higher energies in experiments in which electrons are added to a system with low screening efficiency. This is actually the case for Fe-O systems where oxygen atoms act as ligands with considerably localized

states, as it has been thoroughly discussed for bulk FeO [48]. Similar effects could well be at the basis of the present STS findings when the tunneling current injected into the surface is increased. A deeper understanding of the observed shifts would of course benefit from simulations of the surface in out-of-equilibrium conditions or in the presence of a strong localized electric field. However, we can conclude that good agreement is obtained if the zero-current extrapolated position E_0=0.83 eV is directly compared to the computed energy position of the surface state (0.83 vs 0.8 eV). Physically, we can interpret this limit as corresponding to infinite tip-sample distance, i.e., unperturbed system.

1.6 Surfactant effect

Fig. 1.15 reports STM topography images obtained on Fe(001) and Fe(001)-$p(1 \times 1)$O surfaces after room temperature deposition of 0.25 and 3.5 monolayers (ML) of iron (1 ML = 0.143 nm). The early stages of growth are characterized by the same morphology, while the topography of the two surfaces is quite different at higher coverage. After a few monolayers of iron are deposited on the clean Fe(001) surface we observe a typical mound structure [49, 50] with four layers exposed in Fig. 1.15(c). On the other hand, when the same amount of iron is deposited on Fe(001)-$p(1 \times 1)$O, the surface presents only two exposed layers. The wedding-cake structure observed in Fig. 1.15(c) is replaced in Fig. 1.15(d) by single-layer islands covering about half a layer. Fig. 1.16 shows the progression of the surface morphology during Fe homoepitaxy on Fe(001)-$p(1 \times 1)$O in the submonolayer coverage range.

The lowest coverage is characterized by a high density of circular-shaped islands. When the coverage is increased, these islands coalesce forming a percolation network. Further deposition of iron causes the completion of the growing layer before the next layer begins to nucleate, confirming the well-known layer-by-layer growth mode of Fe on Fe(001)-$p(1 \times 1)$O and the surfactant action of the oxygen atoms chemically bound to the Fe(001) surface [51]. In principle, two distinct conditions must be fulfilled in order to have a surfactant action. First, the surfactant atoms must be able to float on the surface during the growth. In this respect it is important to establish whether the oxygen is present at the surface of the growing islands or whether it floats only after the layer is completed. An inhomogeneous oxygen distribution can in fact lead to a different diffusion rate of the atoms landing on the substrate or on an island, influencing in this way the morphology of the growing surface. Fig. 1.17 displays STM and STS data measured on the region straddling an island grown on the Fe(001)-$p(1 \times 1)$O surface [panels

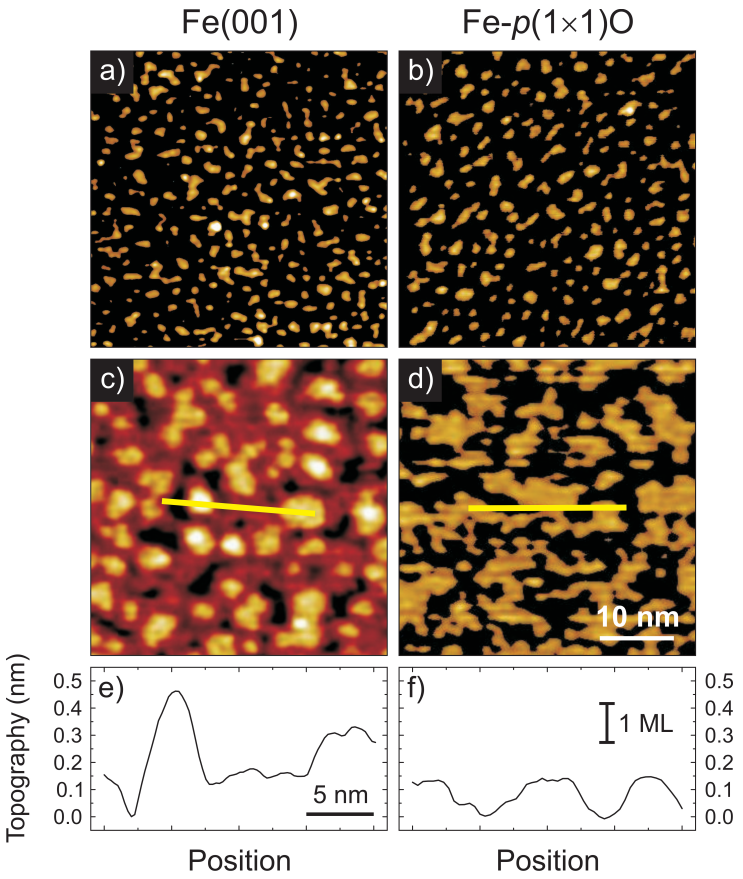

Figure 1.15: (Color online) STM topography after deposition of 0.25 ML of iron on Fe(001) (a) and Fe(001)-$p(1 \times 1)$O (b). STM topography after deposition of 3.5 ML of iron on Fe(001) (c) and Fe(001)-$p(1 \times 1)$O (d). (e) and (f) STM profile measured along the lines traced in panel (c) and (d), respectively.

(a) and (b), respectively]. The STS spectra collected on the substrate and on the islands are very similar, presenting the typical spectroscopic features observed on a freshly prepared Fe(001)-$p(1 \times 1)$O surface, located at roughly 1 eV above the Fermi energy (E_F) and 0.5 eV below E_F [31]. This demonstrates that the oxygen atoms float on top of the surface, as also confirmed by the atomically resolved STM topography in Fig. 1.17(a). In this figure, the same (1×1) symmetry with a corrugation of about 30 pm, typical of Fe(001)-$p(1 \times 1)$O [31], is observed on both the substrate and the island [note that the atomic corrugation on clean Fe(001) is smaller than 2 pm, i.e., below our vertical sensitivity]. The second condition for the adsorbed atoms to exhibit a surfactant action is that their presence should enhance the ratio between the interlayer and intralayer mass transport efficiency. The surfac-

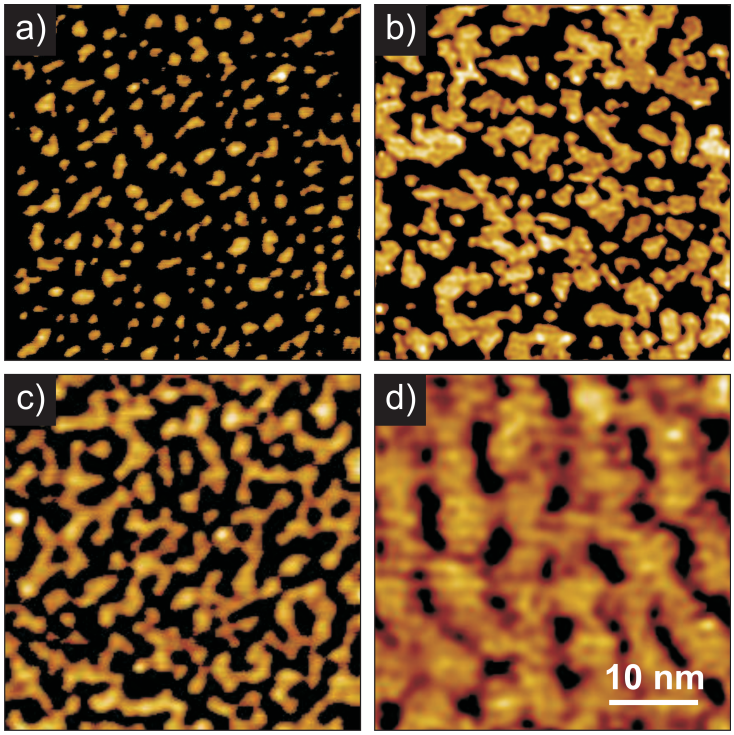

Figure 1.16: (Color online) Surface morphology for increasing coverage of iron on Fe(001)-$p(1 \times 1)$O: (a) 0.25 ML, (b) 0.5 ML, (c) 0.7 ML, (d) 0.85 ML.

tant can affect this ratio by either (i) increasing the interlayer mass transport or (ii) decreasing the intralayer mass transport. In the first case, the surfactant atoms directly lower the potential barrier at the step edges (Schwoebel barrier) without changing the diffusion coefficients within a given layer. In the second case, the surfactant hinders the intralayer diffusion, usually leading to a very high density of small islands in the first stages of nucleation [52, 53]. The importance of this effect can be appreciated by considering that reducing the sample temperature can change the growth mode even in the absence of any surfactant, increasing at the same time the number of islands in the very first stages of growth. The island average size can significantly affect the growth mode because atoms deposited on smaller islands have a higher attempt frequency to overcome the potential barrier and descend on the lower layer. Moreover, the nucleation of a second layer is less probable on top of a smaller island due to the reduced number of successive arrivals of atoms [52, 53]. Generally speaking, the surfactant action can change both the intralayer and the interlayer mass transport. While cases have been reported in which the surfactant changes the intralayer diffusion leaving substantially unchanged the interlayer mass transport [52, 53], the

reverse situation has not been observed so far. For instance, oxygen-induced lowering of the potential barrier at the step edges has indeed been observed on the Pt(111) surface covered by an ordered $p(2 \times 2)$ oxygen overlayer [54]. In that case, however, the intralayer diffusion was also significantly modified by the presence of oxygen, as testified by the fact that the island density is 16 times larger on the oxidized surface than on clean Pt(111). Surprisingly, we found that in our case the intralayer mass transport is not affected by the presence of the surfactant. Inspection of Figs. 1.15(a) and 1.15(b) indicates that the density, shape, and average size of the islands forming during the first stage of Fe growth on either Fe(001) or Fe(001)-$p(1 \times 1)$O are essentially the same, which means that the intralayer mass transport is substantially unaffected by the presence of oxygen on the surface. In fact, in the pristine Fe(001) surface, we measured an island density equal to 0.18 nm^{-2} (standard deviation is 0.001 nm^{-2}) and an island average size of 1.41 nm^{-2} (s.d. = 0.12 nm^{-2}). In the Fe(001)-$p(1 \times 1)$O surface the island density is 0.16 nm^{-2} (s.d. = 0.001 nm^{-2}) and an island size of 1.56 nm^{-2} (s.d. = 0.17 nm^{-2}). Note that in cases where surface diffusion is significantly reduced by the presence of a surfactant, the island density in the early stages of nucleation on the surfactant-covered surface is orders of magnitude larger than that of the clean surface. We thus deduce that oxygen shows surfactant properties by increasing the efficiency of interlayer mass transport. This conclusion differs from that proposed in Ref. [7], where it was suggested that the oxygen surfactant action could be similar to that of Pb during the homoepitaxial growth of Cu on Cu(111) [52]. In this case, easy incorporation of incoming Cu below the Pb layer inhibits intralayer diffusion, while interlayer transport, promoting layer-by-layer growth, still occurs by exchange with atoms at the borders of nucleated islands and is only slightly influenced by the presence of the surfactant [52]. In this way the ratio between interlayer and intralayer mass transport is enhanced and the layer-by-layer growth established. In our case, STM analysis allows us to rule out that oxygen significantly affects intralayer mass transport, suggesting that the oxygen does not change the diffusion mechanism within the terrace, and that the surfactant action is solely due to a reduction of the Schwoebel barrier. To give a possible explanation of the Schwoebel barrier lowering, we briefly recall the atomistic mechanisms involved in the interlayer diffusion. An atom arriving at the island edge can cross the step by either hopping over the step or pushing out one edge atom [55]. Generally, the second mechanism (also known as exchange process) is the most efficient one in the case of homoepitaxy and heteroepitaxy of metals [52, 55]. As discussed previously, when we deposit iron on the Fe(001)-$p(1 \times 1)$O surface the growing islands are under compressive stress due to the chemisorbed oxygen. Compressive stress is known to

induce a lateral relaxation of the edge atoms, which is proven to favor the exchange process, e.g., during the growth of Ag on the (111) surfaces of Ag and Pt [56, 57]. We thus propose a link between the oxygen-induced stress and the enhanced interlayer mass transport.

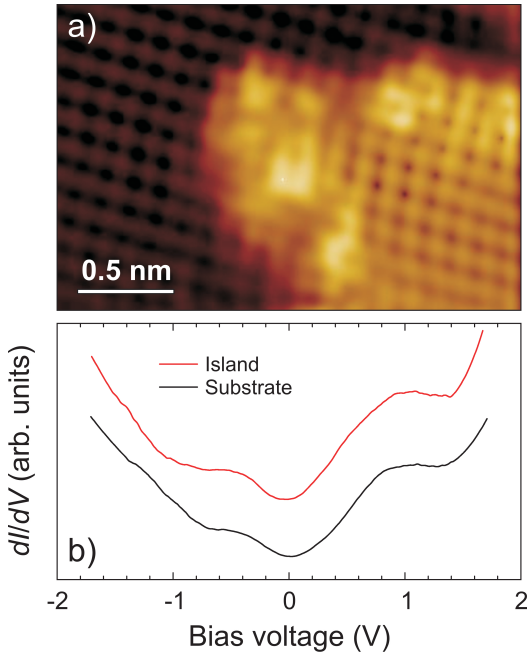

Figure 1.17: (Color online) (a) STM topography on a region straddling the Fe(001)-$p(1 \times 1)$O substrate (dark) and an island (bright) formed upon Fe evaporation. (b) STS spectrum measured on the island. Both substrate and island are characterized by the same (1×1) corrugation and STS spectrum.

Chapter 2

Oxygen mediated $3d$ metals/Fe(001) interfaces

2.1 Introduction

Thin films of metals epitaxially grown on metals have attracted sustained scientific and technological interest for more than half a century.

The structural and morphological stability of ultrathin heteroepitaxial films is strongly dependent on a number of factors like the strain induced by lattice mismatch, the kinetics conditions of growth and the presence of adsorbates on the substrate [58].

In particular, magnetic thin films and superlattices can be characterized by new magnetic phases and exotic magnetic couplings. In this frame the interfaces between Cr/Fe(001) and metastable Ni/Fe(001) are prototypical examples of such kind of systems.

The Cr/Fe(001) system was extensively studied in the past [59, 60, 61, 62], particularly by focusing on the surface morphology and on the chemical interactions occurring at the interfaces. The use of Fe/Cr/Fe as a model system made possible significant progress in the understanding of the phenomena of exchange coupling between ferromagnetic layers separated by a nonmagnetic layer [63]. In this kind of structures it is crucial to obtain abrupt interfaces and smooth surfaces, because the magnetic properties are strongly influenced by the chemical composition and by the structure of such interfaces. Layer by layer growth has been obtained by growing at high substrate temperature (T=570 K). Such an approach, on the other hand, was affected by a relevant problem, namely interface alloying between Fe and Cr [61, 62]. The latter was greatly enhanced by the high deposition temperature, and has been thought to be responsible for a phase shift observed in the magnetic ordering

of the chromium layers. An alternative to high temperature deposition could be the use of the surfactant.

In the field of ultrathin magnetic films, metastable body-centered-cubic (bcc) phase of nickel has attracted great interest in the past [70, 71]. The only phase observed at normal temperature and pressure in bulk Ni crystal has the face centered cubic (fcc) structure, but metastable bcc phase has been stabilized both on magnetic or non magnetic substrates [70, 71, 72]. Thin epitaxial Ni films grow pseudomorphically on the Fe(001) with a bcc structure and in a layer by layer mode for few layers [69]. The magnetic properties of these bcc Ni ultrathin films strongly depends on parameters like the interlayer spacing, film roughness and hybridazation with the substrate [73]. For instance it is predicted theoretically that bcc Ni at equilibrium (with a lattice constant of 0.2773 nm) would be paramagnetic, but a transition to a ferromagnetic state would occur upon expansion of the lattice beyond 0.2815 nm [73].

In this respect it is interesting to investigate the oxygen induced effects on the nickel films grown on the Fe(001) surface. In fact, it has been demonstrated that a single layer of chemisorbed oxygen on the Fe(001) causes a strong relaxations of the topmost layers [9, 10, 11, 12, 13], giving rise to phenomena like enhanced surface magnetic moment [4] and surfactant action [5, 6, 7].

In this chapter will discussed the oxygen induced effects on the Cr/Fe(001) interface and on the Ni/Fe(001) interface.

In the section 2 the oxygen-aided growth of thin Cr film on the Fe(001) substrate will be discussed, and in particular the temperature dependence of the oxygen surfactant action. What we found is that when the Cr film is grown at 400 K the oxygen overlayer chemisorbed on the Fe(001) surface acts as a surfactant, inducing a smoother growth with respect to the case of the oxygen free Fe(001) substrate.

In the section 3 we will analyze the oxygen mediated Cr/Fe ordered surface alloy, obtained during high temperature deposition of Cr on Fe(001)-$p(1\times1)$O. When the film is grown at 600 K we found that in the submonolayer range an ordered oxygen mediated alloy with a structure $c(2x4)$ is formed. Increasing the coverage up to about 1.2 monolayer leads to the stabilization of a strained $(\sqrt{5}\times\sqrt{5})R27^\circ$ phase, related to the presence of Cr vacancies.

The section 4 is about the oxygen mediated Ni/Fe(001) interface. In the case of Ni deposition on the oxygen passivated Fe(001) we observed an "antisurfactant" effect. When Ni is deposited on the oxygen free Fe(001) it forms a wetting layer and the growth is layer by layer up to 6 ML. On the other hand in the first stages of growth of nickel films on the Fe(001)-$p(1\times1)$O we find that there is the formation of bi-layer islands and the

growth is Volmer-Weber like. Increasing the coverage up to of 5-6 monolayer leads to the stabilization of a strained $(\sqrt{5} \times \sqrt{5})R27^\circ$ phase.

2.2 Oxygen aided growth of Cr on Fe(001)

The first set of depositions was performed at a substrate temperature of 380 K. Fig. 2.1 compares the topography of the sample after sub- and multi-layer deposition on both Fe(001) and Fe(001)-$p(1 \times 1)$O surfaces.

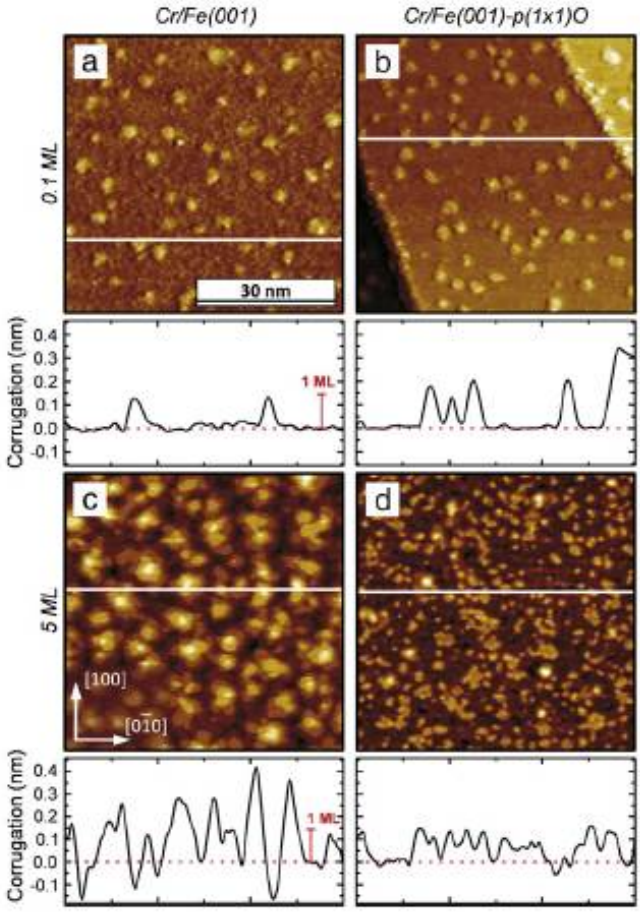

Figure 2.1: Topographic images of Cr films grown at 380 K on the Fe(001) [panels (a) (c)] and on the Fe(001)-$p(1 \times 1)$O [panels(b) and (d)] substrates. The coverage is about 0.1 ML in panels (a) and (b) and about 5 ML in panels (c) and (d). Images have been shaded (light source on the right) to enhance small details. The scale bar apply equally to the four images.

No striking differences can be observed when comparing oxygen free

Fig. 2.1(a) and oxygen covered surfaces Fig. 2.1(b), in the case of sub-monolayer (0.1 ML) Cr growth, in terms of island density [about 18×10^{-11} islands/cm^2 in Fig. 2.1(a), compared to 27×10^{-11} islands/cm^2 in Fig. 2.1(b)] and shape. In both cases, the completion of the first monolayer is seen to proceed via the formation of nucleation centers at the early stages of growth and after (not shown) via the growth of islands and their coalescence when increasing the coverage in the sub-monolayer regime. Multilayer Cr growth on the Fe(001) substrate then proceeds via the formation of mounds [Fig. 2.1(c)]. This phenomenon is related to the presence of a barrier at the edges of steps and islands, called Ehrlich Schwoebel (ES) barrier, which increases the residence time of adatoms on the islands, thus increasing the probability of formation of new nuclei on top, as reported for iron homoepitaxy. At variance with the situation seen in Fig. 2.1(c), panel (d) shows that the presence of an oxygen layer on the substrate promotes a layer by layer growth. This conclusion is evidenced by considering the horizontal line profiles reported below the STM images in Fig. 2.1. In particular, the corrugation profile related to panel (c) features steps as high as 2 or 3 ML, while the one related to panel (d) reveals the presence of only 1 ML high islands, meaning that the growth is proceeding by layers. Fig. 2.2 reports as-measured XPS spectra of the O 1s core level region from the Fe(001)-$p(1 \times 1)$O surface (black squares) and from a 5 ML Cr film on Fe(001)-$p(1 \times 1)$O (red circles). The peak on the left is part of the L_3VV Auger signal from iron.

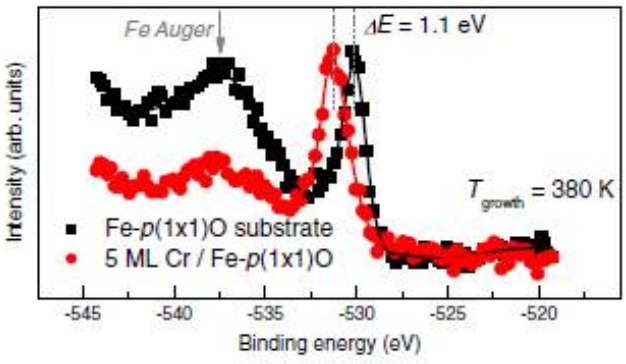

Figure 2.2: Photoemission spectra of the O 1s core level region from the Fe(001)-$p(1 \times 1)$O substrate (black squares) and from a 5 ML Cr film on Fe(001)-$p(1 \times 1)$O (red circles) grown with a substrate temperature of 380 K. The Fe Auger peak (see text) is indicated by an arrow. The solid lines are guides to the eyes.

The comparison between these spectra reveals that the intensity of the Auger signal is reduced, as expected from electron attenuation through the Cr film, while the intensity of photoemission from oxygen is not reduced.

This result demonstrates that oxygen atoms segregate to the topmost layers, thus creating an oxygen-enriched region where the surfactant action takes place [64]. Oxygen can therefore be considered responsible for the different type of growth observed in Fig. 2.1(c) and in Fig. 2.1(d), respectively. The energy shift in the O 1s peak position, which amounts to 1.1 eV, can be understood as a result of the different chemical bonding experienced by the oxygen atoms on the Cr surface.

The second set of depositions was performed at 570 K. Fig. 2.3 shows the surface topography after the deposition of 0.4 ML (panels a and b) and 5 ML (panels c and d) of chromium.

For what concerns sub-monolayer deposition, we observe that the density of islands in Fig. 2.3(a), referring to Cr deposition on a pristine Fe(001) surface, is evidently higher than in Fig. 2.3(b), which refers to Cr deposition on the Fe(001)-$p(1 \times 1)$O surface. In both cases, the islands retain a rounded shape, due to the enhanced mobility of edge adatoms, which allows for the healing of corners at the island's sides during growth. Furthermore, a part of the deposited atoms have diffused toward step edges, which are characterized by the same rounded profile as the islands. Fig. 2.3(c) and (d) show the sample morphology after the deposition of 5 ML of chromium on the Fe(001) surface [panel (c)] and on the Fe(001)-$p(1 \times 1)$O surface [panel (d)] at 570 K. While deposition on the oxygen free substrates yields a layer by layer growth (see the horizontal line profile below the figure) with rounded islands and edges, the surface morphology of panel (d) is dominated by mounds with a square like base and the shape of a step pyramid. Many of the mounds include a spiral core, as shown in the inset. Spirals are separated by deep grooves, and are reminiscent of the mounds structure of Fig. 2.3(c). The significant differences in terms of Cr surface morphology between the lower and the higher growth temperature cases do not find a correspondence when analyzing XPS results. In particular, the spectra line shapes for Cr 2p and Fe 2p core levels (not shown), are almost unchanged when measured on the 5 ML Cr/Fe(001)-$p(1 \times 1)$O samples obtained in the two growth regimes. Similar observations can be made when inspecting the O 1s core level region. Fig. 2.4 reports as-measured XPS spectra of such a region, and compares the Fe(001)-$p(1 \times 1)$O surface (black squares) and a 5 ML Cr film on Fe(001)-$p(1 \times 1)$O (red circles), similar to Fig. 2.2.

Analogously to the lower temperature case, the intensity of the signal due to the photoemission of oxygen core electrons is not reduced. The only small difference is in the peak position, which is shifted to higher binding energies by 0.7 eV instead of 1.1 eV, suggesting possibly a different coordination of the oxygen atoms at the surface. Therefore, it is clear that oxygen atoms still segregate to the topmost layers, even if this does not lead to a layer by

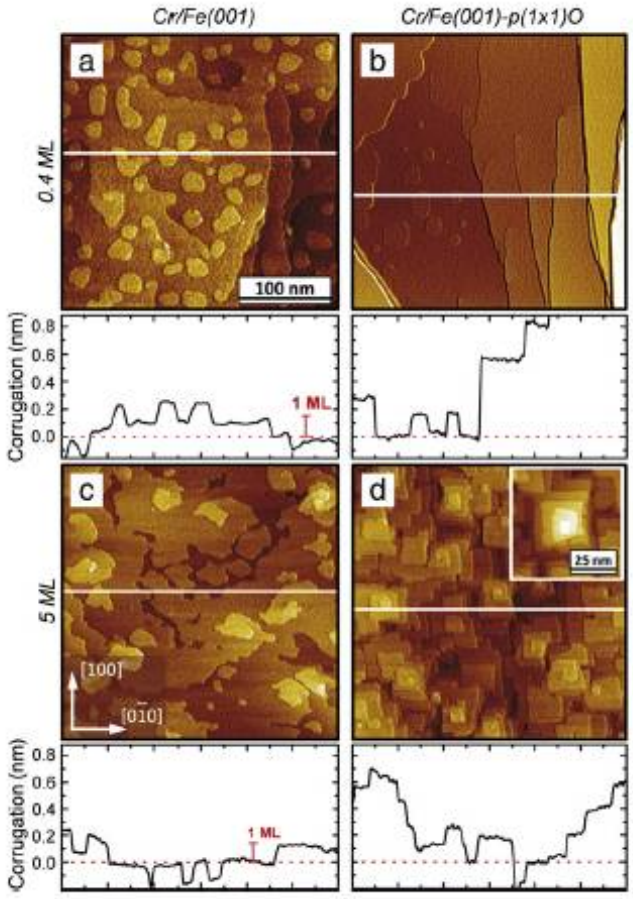

Figure 2.3: Topographic images of Cr films grown at 570 K on the Fe(001) [panels (a) and (c)] and on the Fe(001)-$p(1 \times 1)$O [panels (b) and (d)] substrates. The coverage is about 0.4 ML in panels (a) and (b) and about 5 ML in panels (c) and (d). Images have been shaded (light source on the right) to enhance small details. The scale bar apply equally to the four images. The inset of panel (d) shows a square pyramid; the scale is doubled with respect to the other images.

layer growth in the higher temperature case.

The results presented have shown that the surfactant effect of oxygen on the growth of a Cr film on a Fe surface can be strongly affected by the growth temperature. With reference to the lower growth temperature cases (see Fig. 2.1), we first consider the initial stages of islands nucleation, at sub-monolayer coverages. The most remarkable information that we can obtain by comparing Fig. 2.1 (a) and (b) is the very similar density of islands (about 18×10^{11} islands/cm^2 compared to 27×10^{11} islands/ cm^2). At sub-monolayer coverages, before islands coalescence, we expect that the density of islands

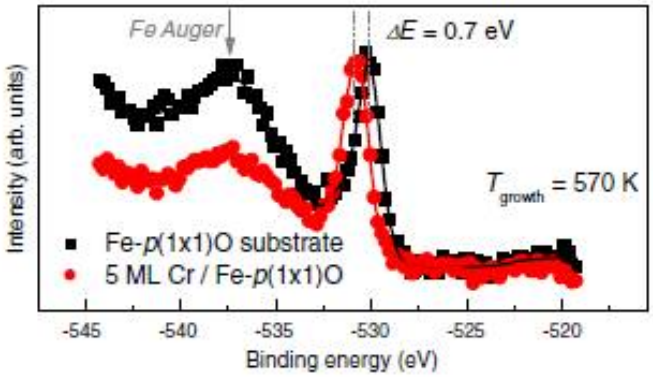

Figure 2.4: Photoemission spectra of the O 1s core level region from the Fe(001)-$p(1\times1)$O substrate (black squares) and from a 5 ML Cr film on Fe(001)-$p(1\times1)$O (red circles) grown with a substrate temperature of 570 K. The Fe Auger peak (see text) is indicated by an arrow. The solid lines are guides to the eyes.

can be related to the deposition rate and to the energy barrier for single atom hopping from one lattice site to the next. Since the deposition rate was the same when growing Cr on top of both the Fe(001) and the Fe(001)-$p(1\times1)$O surfaces, the similar density of islands in panels (a) and (b) of Fig. 2.1 clearly indicates that the oxygen layer does not appreciably reduce the effective diffusion length of Cr adatoms at sub-monolayer coverage. Moreover, our findings imply that the rate of incorporation of adatoms into the surfactant layer is negligible with respect to the rate of islands nucleation at 380 K. If we now consider the early stages of island nucleation for the higher growth temperature cases [see Fig. 2.3, panels (a) and (b)], we observe two dramatically different situations. In the first place, in the case of the oxygen free growth on the pristine Fe(001) surface, we find that the number of sub-monolayer islands in Fig. 2.3(a) is about 8.0×10^{10} islands/cm^2 (i.e. one order of magnitude smaller than in the lower temperature case, see above), consistent with the coverage observed in the literature under very similar growth conditions. In fact, with respect to the adatom hopping mechanism, higher temperatures are expected to increase the diffusion length of adatoms and conversely reduce the density of nucleated islands. A complication could be represented by the presence of terraces, which can perturb the local density of adatoms and reduce the number of nucleated islands by incorporating incoming atoms. A qualitative inspection of Fig. 2.3 (a) reveals anyway that the terrace edges do not seem to perturb the local density of islands upon the terrace (i.e. we do not observe depleted zones on the terrace upper sides), consistently with the existence of the ES barrier, which impedes the mecha-

nism of adatom incorporation into the steps. In the second place, the case of sub-monolayer Cr deposition on Fe(001)-$p(1 \times 1)$O at 570 K is characterized by an evident further reduction of the islands. Fig. 2.3 (b) shows, in particular, that islands are formed only at the bottom of the terrace structure. After extended observations of the sample surface, we can conclude that the mechanism of island nucleation takes place only on wide terraces. This is consistent with a lowering of the ES barrier at the step edges, favoring the interlayer transport of adatoms, as already observed in the case of oxygen aided iron homoepitaxy (see chapter 1). If we now increase the Cr coverage, the evolution of the higher temperature grown Cr/Fe(001)-$p(1 \times 1)$O system leads to surprising results. The addition of surfactants is usually thought to reduce the roughness of the deposited films with respect to the growth on clean substrates. Fig. 2.3 (d), however, shows an unexpected surface evolution, characterized by the presence of spirals. The latter can be understood as the result of the revolution of a step edge around the core of a screw dislocation, which pins the step itself. Growth spirals were also observed during Cr epitaxy on Fe(001) substrates [(Fig. 2.3(c)]. The competition with island formation, however, did not allow for the development of the structure observed during growth on Cr/Fe(001)-$p(1 \times 1)$O substrates, characterized by several turns around the spiral core (at the Cr coverages considered in the present work). In order to have the formation of spirals, the growth mode should change from growth by island nucleation to step flow like, in which adatoms stick directly to the edges, instead of nucleating new islands on the substrate. The transition between the island formation and the step flow regimes is determined by several parameters (see e.g. Ref. [65]). The growth temperature and the presence of screw dislocations (or extended edges in general) on the substrate, for instance, are fundamental ingredients. Regarding the presence of screw dislocations, a qualitative comparison between Fig. 2.3(a) and (c) (oxygen free growth case), and between Fig. 2.3(b) and (d) (oxygen aided growth case) reveals that the number of dislocations on the Cr films is comparable to that on the Fe substrate itself, in both cases. For what concerns the growth temperature, it actually was the same when growing Cr on both the oxygen free and on the oxygen covered substrates (Fig. 2.3 panels c and d, respectively), and lower than the temperature the samples felt during substrate preparation. The major difference between the cases of Fig. 2.3c and d is again the presence of oxygen during growth. Oxygen must therefore play a significant role in determining the three dimensional growth mechanisms that produce Cr spirals at the higher temperature growth. In particular, some parameters that are expected to be influenced by the presence of oxygen are the diffusion coefficient of adatoms and the strength of the atom binding at the edges.

To summarize our experimental results, we have observed that the presence of oxygen on the Fe surface produces a layer by layer growth of ultrathin Cr films on Fe(001) when such a growth is realized at T=380 K. XPS measurements testify that oxygen segregates to the topmost layers and contribute to demonstrate the surfactant action of oxygen. The latter mainly acts through the lowering of the ES barrier at the step edges, favoring the interlayer transport of adatoms, i.e. the filling of the lower layers before nucleating new islands on top of the existing ones. A significantly different morphology is observed when Cr is grown at T=570 K, showing that the oxygen surfactant effect is strongly affected by the substrate temperature. In particular, at variance with the observations reported for the lower temperature case, the growth mechanisms on top of the Fe(001) and of the Fe(001)-$p(1 \times 1)$O surfaces are different already at a sub-monolayer level. Such mechanisms, in the presence of oxygen, lead to a complicated three dimensional growth scenario, characterized by spirals with a square like base. The surfactant effect in such a case is therefore lost.

2.3 Oxygen mediated alloying of Cr on Fe(001): the $c(4 \times 2)$ and $(\sqrt{5} \times \sqrt{5})R27^\circ$ phases

In Fig. 2.3 there is a comparison of the submonolayer deposition of Cr on the pristine Fe(001) and Fe(001)-$p(1 \times 1)$O. When we deposit Cr on the Fe(001)-$p(1 \times 1)$O, the number of nucleated islands is less than that we find when we use as substrate the oxygen free Fe(001). Surprising, for a nominal deposition of 0.4 ML of Cr (as measured from the quartz microbalance calibration), we find that the islands cover only about 0.05 ML. Furthermore, the islands nucleate only on large terraces, indicating that the steps can influence the nucleation process, acting as a sink for the adatoms. In figure Fig. 2.5 there is a microscopic view of the surface. After the Cr deposition we find that the surface is covered by bright spots embedded on the substrate, that are imaged as atomic corrugation (apparent height 50 pm). The bright spot number increases with the Cr deposition and is consistent with the nominal coverage. An interesting feature is that their disposition is somehow ordered. In particular, when the nominal coverage is about 0.4 ML, there are clearly visible regions in which the bright spots form a $c(4 \times 2)$ superstructure.

When the Cr coverage is increased to 0.75 ML the $c(4\times2)$ structure covers the entire surface (see Fig. 2.6), as confirmed also by the LEED pattern (not shown) . After further deposition of Cr, a dramatic change takes place and the overlayer symmetry becomes $(\sqrt{5} \times \sqrt{5})R27^\circ$, characterized also by

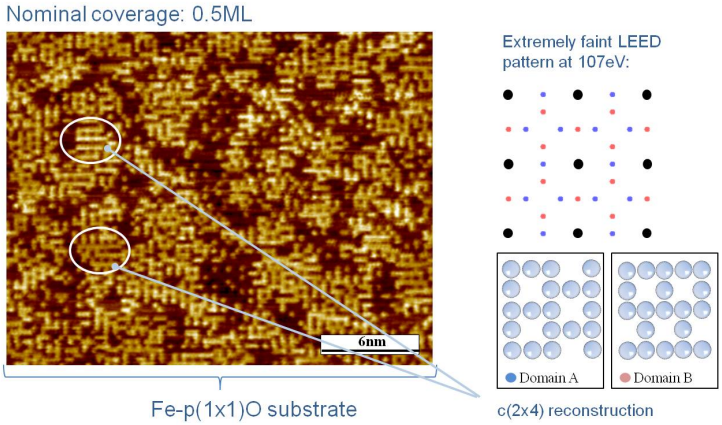

Figure 2.5: Microscopic view of 0.5 ML of Cr deposited on Fe(001)-$p(1 \times 1)$O. The bright spots are measured as atomic corrugation (apparent height 50 pm)

a very sharp LEED. What we observed is that the coverage at which the overlayer structure switches from $c(4 \times 2)$ to $(\sqrt{5} \times \sqrt{5})R27°$ is about 1.2 ML, and that further increase of the Cr film thickness does not change the overlayer structure, even tough the LEED pattern becomes weaker, due to the increased surface roughness and the spiral formation (see the previous section).

The experimental data suggest the formation of an alloyed phase in the submonolayer range. The bright spots are related to the presence of the Cr atoms, even if we do not have the experimental evidence that what we image as protrusion are the Cr atoms. The XPS spectra taken before and after the Cr evaporation (not shown) are unchanged, thus we can state that we still have an oxygen monolayer present on the top of the surface.

Based on this experimental results, we suggest a model in which the Cr atoms replace 3/4 of the iron atoms present in the topmost layer, giving a formal stoichiometry Cr_3FeO_4. Notice that when we deposited Cr at 470 K we were able to reproduce the result of Davies et al. [61] In that case:(i) in the submonolayer range there is a strong Cr interdiffusion into the bulk of the iron and only one out of 4 deposited Cr atoms stays in the surface layer; (ii) the topmost layer is characterized by the formation of a disordered alloy. On the other hand, in the case of Cr deposition on the oxygen passivated surface, what we observed is that: (i) within the experimental error all the deposited atoms remain in the surface layer and (ii) the alloyed phase is well ordered, giving a $c(4 \times 2)$ superstructure.

The interpretation of the $(\sqrt{5} \times \sqrt{5})R27°$ is quite different. In fact, the $(\sqrt{5} \times \sqrt{5})R27°$ phase is present also on the oxygen covered Cr(001) surface

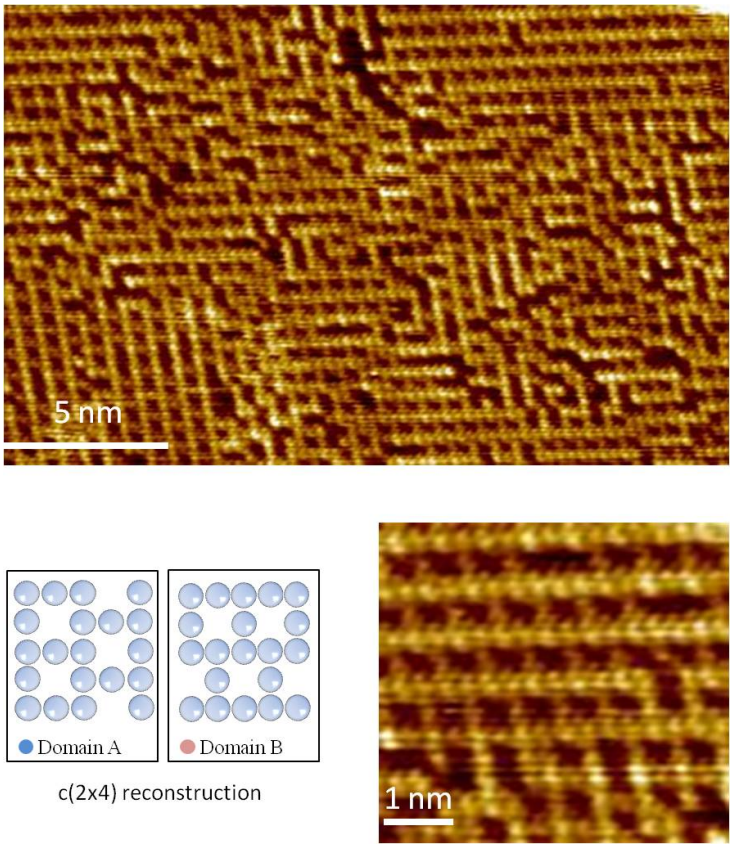

Figure 2.6: The $c(4 \times 2)$ phase obtained after the evaporation of 0.75 ML of Cr on Fe(001)-$p(1 \times 1)$O

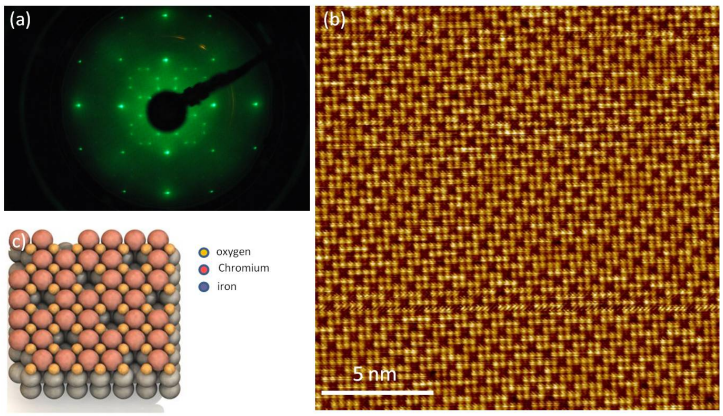

Figure 2.7: The $(\sqrt{5} \times \sqrt{5})R27°$ phase: (a) Leed pattern at 107 eV, (b) atomic resolution and (c) atomistic model

[66], thus we can speculate that in this case the surface is composed only by Cr and oxygen atoms. A model of this surface, based on the work of Schmid [66], is shown in Fig. 2.7. The dark spots are interpreted as Cr vacancies and the stoichiometry in this case is Cr_4O_5.

In conclusion, during the first stage of growth at high temperature (470 K), there is an oxygen mediated Cr/Fe surface alloy, highly ordered and with a $c(4 \times 2)$ symmetry. Increasing the Cr coverage gives the $(\sqrt{5} \times \sqrt{5})R27°$ overlayer. In this case the holes seen in the STM images are interpreted as chromium vacancies, and we can see the system as a Chromium oxide single layer accomodated on the top of the Fe(001) surface.

2.4 Nickel nanolayers on oxygen passivated Fe(001) surface

Nickel films were grown onto Fe(001)-$p(1\times1)$O substrates by molecular beam epitaxy under UHV conditions, with a typical growth rate of about 0.7 equivalent monolayers per minute (where one equivalent monolayer 1 ML equals the amount of Ni atoms required to completely saturate the adsorption sites on the Fe substrate, i.e. about 12.2×10^{14} atoms/cm^2). The sample was heated by resistive heating and its temperature was measured by a thermocouple attached in close proximity to the sample position. The deposition rate was estimated by a quartz microbalance.

Fig. 2.8 shows the STM images taken on a 100×100 nm^2 scale for increasing nickel coverage. The initial nucleation is characterized by flattop islands. The measured island height is found to be about 280 pm [see Fig. 2.8(f)] and is not affected by the tunneling conditions used. Considering that for very thin films nickel grows pseudomorphic on bcc iron and that in the Fe(001) 1 ML corresponds to 143 pm, we can assume that the measured height correspond to 2 ML . The number of single layer islands is negligible (less than 3%).

The diagram in figure Fig. 2.8(e) displays the layer filling of the first 3 layers when the nominal coverage is increased from 0.3 up to 2.5 ML. For a nominal coverage of 0.3 ML the islands are all 2 ML high, with only few nuclei of the third layer (less than 2%). When the nickel coverage is increased, the third layer filling proceeds faster, and for a total coverage of 2.5 ML we find that 80% is covered by islands of 3 ML, and that 20% of the surface is still uncovered.

For 5 ML of nominal coverage the substrate is completely covered by the nickel film, and there are still 3 layers exposed. A remarkable feature is that

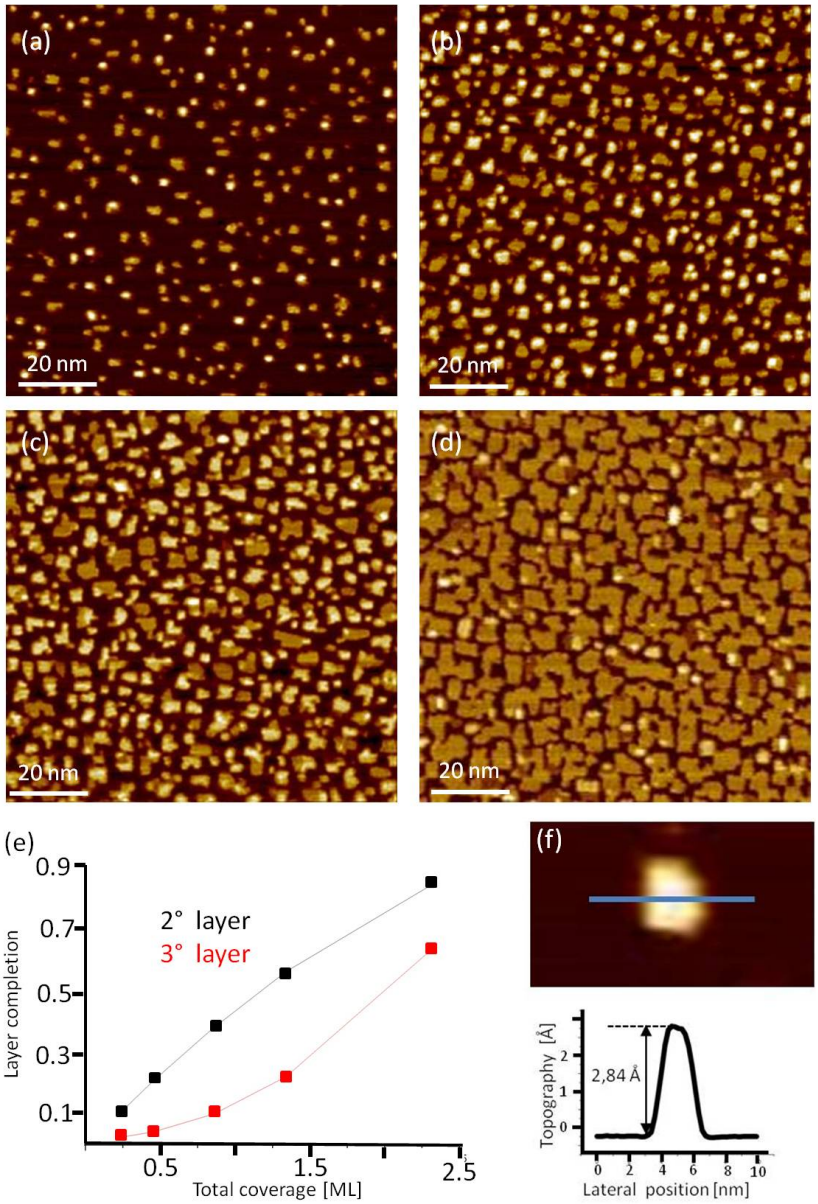

Figure 2.8: STM topography after deposition of (a) 0.3 (b) 0.5 (c) 1.1 (d) 2.4 ML of nickel on Fe(001)-$p(1\times1)$O. Panel (e) shows the percentage of completion of the layers versus the number of equivalent monolayers deposited. (f) STM image of a Ni island 2 ML thick formed after deposition of 3 ML nickel and correspondent topographic line scan.

the topmost layer always nucleates at the edges of the islands belonging to the previous layer, forming in this way steps of 2 ML (see Fig. 2.9)

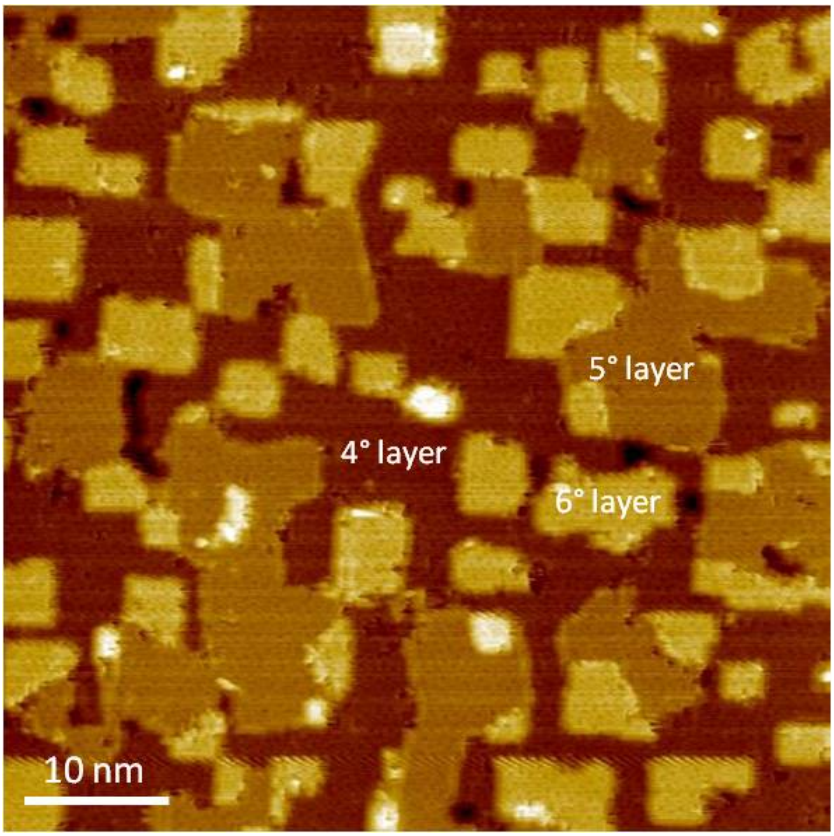

Figure 2.9: STM topography after deposition of 5 ML of nickel. There are 3 layers exposed.The nucleation of the topmost layer is always at the edge of the islands belonging to the previous layer.

Fig. 2.10 displays an atomic resolved image on a region straddling the Fe(001)-$p(1 \times 1)$O substrates and an island 3 ML high. The substrate and the islands have both a square symmetry, but on the top of the island some randomly distributed holes are visible. These holes are measured by STM as depressions 30 pm deep and occupy the equivalent lattice sites of the islands in which protrusions are visible. In order to see the geometric relation between the bright spots of the substrate and of the island we have drawn parallel lines crossing the island edge [see Fig. 2.10(b)]. The result is that the bright spots of the substrate are aligned to the bright spots of the islands.

When the substrate is completely covered by nickel the order of the holes increases and some patches of $(\sqrt{5} \times \sqrt{5})R27°$ reconstruction (Fig. 2.11) are clearly visible. The order of this superstructure is too weak to result in well-defined peaks in either the Fourier transform of the STM image or the LEED pattern.

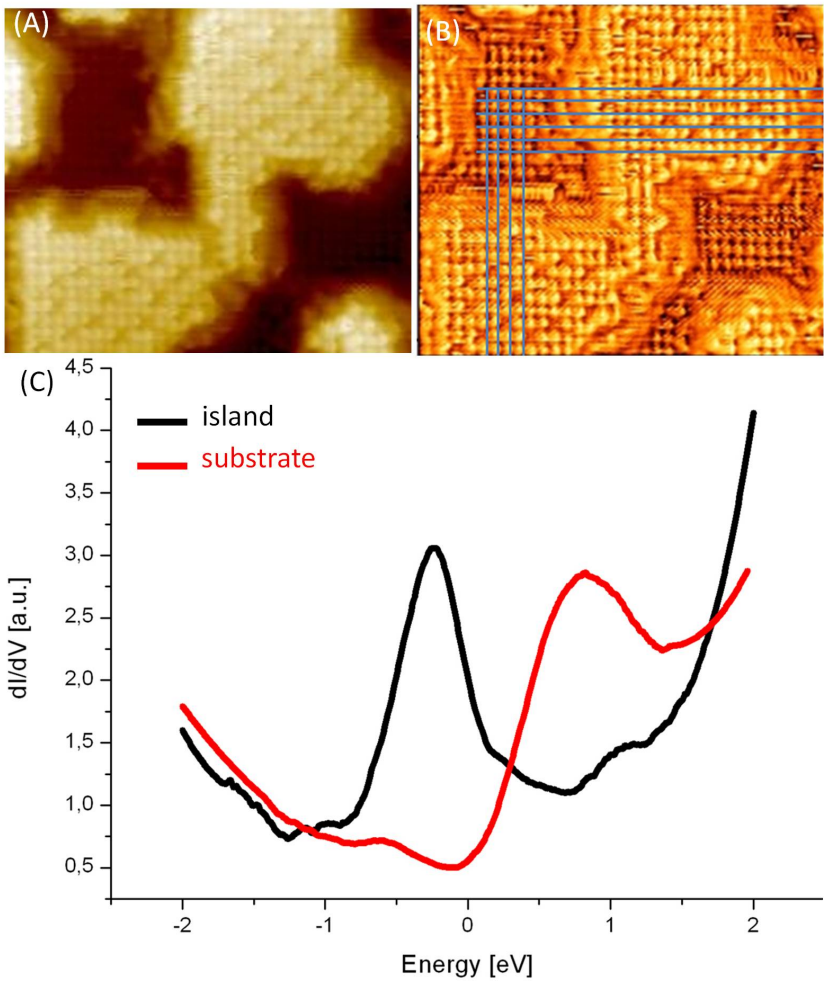

Figure 2.10: (a)(b) Atomic resolved image on a region straddling the Fe(001)-$p(1\times1)$O substrate (dark) and a nickel island (bright) 3 ML high. The bright spots on the substrate are aligned with the bright spots on the island. (c) STS spectra measured on the island and on the substrate (measurement set-point: current $I_t = 1$ nA, bias $V_b = 1V$).

After every nickel deposition we measured the Auger spectra, and the magnitude of the oxygen signal was found unaffected by the presence of the nickel film, indicating that the oxygen is always floating at the top of the growing film. In the coverage investigated the LEED pattern (not shown) was always (1×1), confirming that Ni has a bcc structure.

In Fig. 2.10 are shown the STS spectra acquired on the Fe(001)-$p(1\times1)$O substrate and on top of the nickel islands. The STS curves on the substrate have the characteristic feature of the Fe(001)-$p(1\times1)$O, located about 0.8 eV

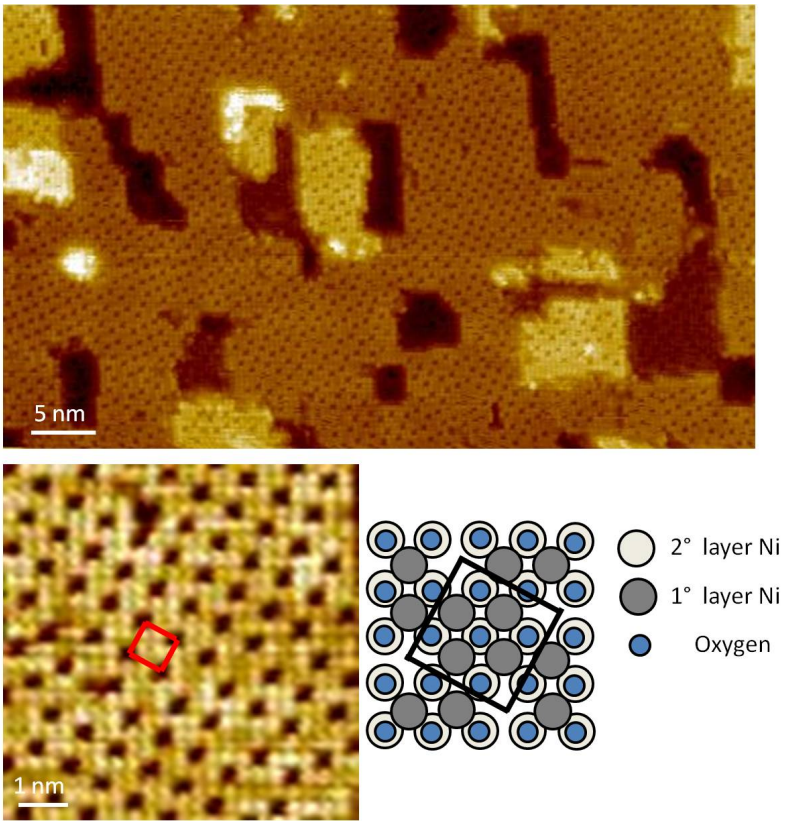

Figure 2.11: (a) Atomic resolved STM image of the surface resulting from the deposition of 5 ML of Ni on Fe(001)-$p(1 \times 1)$O (b) zoom in which it is marked the unit cell of the $\sqrt{5}x\sqrt{5}R27$. (c) Atomistic model of the surface.

above the E_F. The electronic structure of the nickel islands is quite different and there is a peak located 0.2 eV below the E_F. This peak is present since the first stages of nickel growth and we did not observe any difference between the spectra measured at different coverages.

We have also investigated the effect of the thermal treatments after nickel deposition. Thermal treatments do not change the island structure up to a temperature of 600 K. On the other hand, the morphology resulting after a post annealing at 600 K shows dramatic changes. Fig. 2.12 displays the topography obtained after the post annealing of a sample with a nickel coverage of 0,6 ML. The area of the islands increases by a factor 3 and the height becomes equivalent to a single layer of iron (143 pm). A closer look at the surface reveals small-scale features on both the substrate and island levels as shown in Fig. 2.12(b). These bright spots have an apparent height of 40 pm. Furthermore the STS spectra measured both on the substrate and on the is-

lands have the characteristic spectroscopic features of the Fe(001)-$p(1\times1)$O.

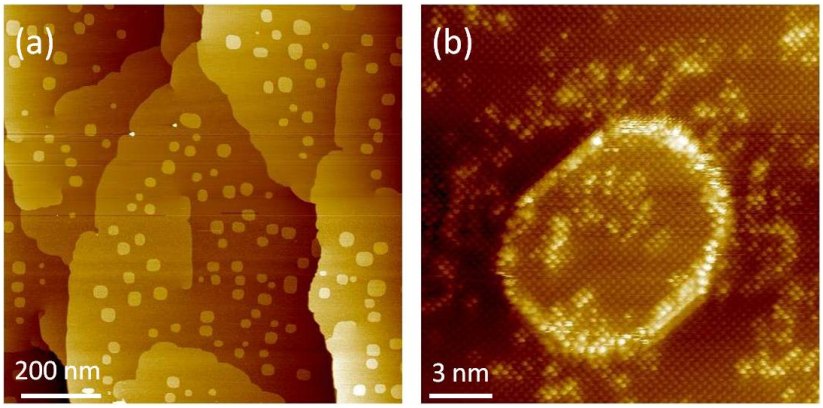

Figure 2.12: Morphology of the post annealed sample at 600 K for a coverage of 0.6 ML: (a) the island size increases by a factor 3. (b) The small bright features on the substrate and on the islands indicate a formation of a surface alloy.

The oxygen surfactant properties have been extensively studied in the past, both in heteroepitaxy and homoepitaxy. We recently studied the atomistic mechanisms involved in the oxygen-assisted growth of iron and chromium on the Fe(001), where the presence of a compact layer of chemisorbed oxygen has been demonstrated to change the growth from a three-dimensional to a two-dimensional mode [67, 68]. In these cases the effectiveness of the oxygen surfactant action has been related to an oxygen induced change in the the growth kinetics, in particular to a lowering of the interlayer mass transport barrier (see chapter 1).

In the case of the oxygen assisted growth of nickel on Fe(001) surface the situation is completely reversed. Pseudomorphic bcc nickel grows on the oxygen free Fe(001) in a layer by layer mode up to 6 layers [69]. Our STM measurement performed on the nickel films grown on oxygen free Fe(001) confirm these results, and in particular show that the islands in the submonolayer are all 1 ML high. On the other hand, when the nickel is grown on the oxygen passivated Fe(001)-$p(1\times1)$O, the structure is still bcc, as indicated by the (1×1) LEED pattern, but the film does not wet the Fe(001)-$p(1\times1)$O substrate and the oxygen promotes the islanding.

The formation of islands of bilayer height in metal-on-metal heteroepitaxy has been reported in very few cases (see for example [98, 99]). The interpretation of this nonconventional growth mode has been given in terms of: (i) strain relaxation or (ii) electronic effects. In the first case there is a critical thickness below which the islands are thermodynamically forbidden due to the insufficient stress relaxation upon clustering. In the second case

there is an height selection associated with electron confinement as a factor in structural and morphological stabilization of ultrathin films [100].

We suggest that in our case the stress related effects can play a major role. Oxygen induced compressive stress on metal surfaces are well documented in many systems. In the case of Ni(001), the adsorption of 1/4 and 1/2 monolayer of oxygen [corresponding to $p(2 \times 2)$ and $c(2 \times 2)$ reconstruction] turns the intrinsic tensile stress of the clean surface in a compressive one, inducing an upward relaxation of the topmost layers. Furthermore in our case the oxygen coverage is one monolayer, so it is reasonable that this effect is enhanced and that the nickel layers are considerably relaxed with respect to the oxygen free case.

The experimental data presented support this interpretation. First of all the fact that since the early stages of nucleation all the islands are 2 ML plateau-like rules out the possibility that the observed 3D growth is due to a combination of random deposition and kinetic limitations. Furthermore the nucleation of the topmost layer at the edges of the islands belonging to the previous layer indicate the tendency to form as high as possible steps, in order to efficiently relief the accumulated strain. Another feature supporting this interpretation is the nature of the holes giving the $(\sqrt{5} \times \sqrt{5})R27^\circ$ superstructure. In the tunneling conditions used, the bright spots on the Fe(001)-$p(1 \times 1)$O correspond to the oxygen atoms [74], thus if we consider the packing of the bcc structure, we can infer that the bright spots on top of the islands correspond to nickel atoms. The holes are therefore located into the equivalent lattice site of the nickel atoms and could be associated to nickel vacancies. Ordered metal vacancies have already been observed in other oxygen-on-metal systems (see for instance [66, 101]), and their presence has been interpreted in terms of compressive strain relief [in the case strained $C(4 \times 2)$ phase formed by cobalt oxide on Pd(100)] or due to electronic effects [in the case of chemisorbed oxygen on Cr(001) surface [66]]. In our case the strain induced vacancy formation is the most likely one. In this frame, the metal vacancies contribute to relieve the compressive stress due to the presence of oxygen.

Now we discuss the electronic structure of the sample. The observed spectroscopic features suggest that when the film is grown at 400 K there is no surface alloy formation between nickel and iron, and the Fe(001)-$p(1\times1)$O substrate is not influenced by the nickel islands. The peak located 0.2 eV below E_F level observed in the STS curves taken on the top of the growing island and on the complete nickel film could be related to the metastable bcc phase of nickel. A bcc surface state near the Fermi level can be observed also in the tunneling spectra of Fe(001) and Cr(001) surfaces and band-structure calculations have shown that this state is a general characteristic of (001)

surfaces [35], so we speculate that the origin of this peak is the same also in this case.

The last topic that has to be discussed is the stability of the nickel island depending on the post annealing temperature. The islands are unchanged up to a temperature of 600 K, indicating that the bi-layer structure is the most stable one. On the other hand, the structure observed after annealing at 600 K can be related to a strong interdiffusion of the nickel film into the iron bulk, as reported for the Ni films grown on the oxygen-free Fe(001) surface.

In summary, in this section we have investigated by means of scanning tunneling microscopy and spectroscopy the morphology and the electronic structure of ultrathin Ni films grown on Fe(001)-$p(1 \times 1)$O.

In the range of coverage investigated (up to 5 ML) ,Ni grows pseudomorphic with bcc structure. The oxygen floats on top of the growing film and induces, since the first stages of growth, the formation of two monolayer thick islands.

For higher coverages a $(\sqrt{5} \times \sqrt{5})R27^\circ$ superstructure it is stabilized, due to the presence of Ni vacancies. STS spectra show that the electronic structure of the Ni film is dominated by a state located 200 meV below the E_F, likely related to the bcc phase of Ni.

The islanding and the presence of Ni vacancies are explained in terms of the oxygen induced compressive stress. In this respect oxygen is expected to induce a strong relaxation in the Ni films.

Due to the fact that the magnetic properties of thin films strongly depend on the interlayer spacing we we suggest that the observed structure of nickel film could be related to different magnetic properties with respect to the bcc nickel films stabilized on the oxygen free Fe(001) surface. Further experiments along this line are needed to confirm this interpretation.

Chapter 3

Cobalt oxide nanostructures: thin films and nanowires

3.1 Introduction

Low-dimensional oxide nanostructures supported on well-defined metal surfaces have been the subject of intensive study because of their relevance both in fundamental physics and in technological applications [75, 76].

In technological applications they are employed as support surfaces in the field of heterogeneous catalysis [77], in the field of digital data storage and spintronics [78], as dielectrics in gas sensors, to name just a few.

At a more fundamental level, there are a number of scientific challenges associated with oxide nanostructure. These include understanding the nature of oxide surface structures, surface electronic properties and the magnetic properties of oxide surfaces [79].

The low co-ordination number, the reduced symmetry, the strain induced by mismatched substrates, the possibility to stabilize metastable states, and the presence of interface or surface states can profoundly alter the electronic and magnetic properties of thin films or surfaces with respect to the bulk, giving the possibility to create new classes of hybrid systems with tunable physical and chemical properties.

Among the experimental STM studies related to thin films of AFM transition metal oxides that can be found in the literature [86, 87, 88, 89], only a few deal with AFM films in contact with FM materials [90, 91]. Among the AFM materials, late $3d$ transition metal (TM) monoxides (MnO, FeO, CoO, NiO) are particularly important thanks to their appealing properties such as the relatively high Nel temperature, the chemical and mechanical stability, the low lattice mismatch with respect to the corresponding FM metals

and their alloys, and the large electronic gap. The use of AFM transition metal oxides in such systems ensures that indirect exchange interactions due to conduction electrons do not play any significant role in determining their magnetic properties. The latter must then be determined only by direct exchange among nearest neighbors in the AFM film and at the FM/AFM interfaces. On the other hand, many experimental investigations have clearly shown that the magnetic behavior of FM/AFM systems depends on the interplay among a large number of physical phenomena, including chemical interactions [82], low dimensionality [83], strain [84], and morphology [85].

In section 3.2 the nanometer scale morphology of CoO thin films coupled to Fe(001) substrates and the surface topography of subsequently grown Fe/CoO/Fe(001) layered structures are investigated. We observe that, since the early stages of interface formation, the room temperature growth of CoO proceeds in the VolmerWeber mode (three-dimensional islands). After about 5 nominal CoO atomic layers, the substrate is completely covered by CoO and the growth subsequently proceeds in the layer-plus-island mode. The resulting surface morphology is preserved by the upper Fe layer, for thicknesses up to a few nanometers. Furthermore, we discuss the role of the chemical interactions acting at the CoO/Fe interface, in particular observing a clear correspondence between the presence of the CoO islands and the development of iron oxides layers that preferentially form below such islands. Finally, we comment on the possible relationships between morphologic and magnetic properties in our Fe/CoO/Fe layered structures.

In section 3.3 preliminary results about self assembled CoO nanowires on stepped Pd(1 1 19) vicinal surfaces are presented. Quasi one dimensional structures of cobalt oxide can be obtained by means of step decoration of the Pd(1 1 19) surface. This procedure leads to a periodic kinked structure of the steps, with a periodicity corresponding to 9 atomic lattice constant of Pd. The electronic structure of the surface is dominated by a surface state located 200 meV below the E_F. This state is present both on the Pd(001) terraces and in the cobalt oxide nanowire, with a remarkable difference in the intensity.

3.2 CoO/Fe(001) and Fe/CoO/Fe(001) layered structures

A recent investigation by means of Low-Energy Electron Diffraction (LEED) and X-ray Photoemission Spectroscopy (XPS) [92] showed the possibility of growing good quality thin epitaxial CoO films on Fe(001) substrates through

reactive deposition of Co in oxygen atmosphere.

In such a work, in particular, it is shown that room temperature growth of CoO on top of Fe has to be preferred with respect to high temperature growth (usually employed when growing on top of, e.g., noble metals), due to the high chemical reactivity of the CoO/Fe interface. For this reason, we have decided to perform our STM investigation only on samples grown by room temperature MBE. On the other hand, our XPS analysis clearly indicated the formation of various Fe oxides at the CoO/Fe interfaces, in line with other results on similar metal/oxide interfaces [82]. The presence of such oxides at the interface does influence the STM measurements of the CoO thin films, in particular in terms of tunneling mechanisms, as discussed later.

We first consider the Fe(001)-$p(1 \times 1)$O surface on top of the substrate. As seen by STM, such a surface is characterized by wide terraces, that extend many hundreds of nanometers in the [010] direction and many tens of nanometers in the [100] direction. This difference between the two crystallographic directions is most likely due to asymmetries induced by the surface preparation procedure. The surface step heights are typically about 1 nm thick, while monoatomic steps are practically absent. A 250×250 nm^2 STM image of the Fe(001)-$p(1 \times 1)$O surface is reported in Fig. 3.1a), where the features mentioned above are clearly visible.

Panel (b) of Fig. 3.1 reports, on the same scale as Fig. 3.1(a), the morphology of the sample surface after the growth of an amount of CoO equal to a nominal thickness of 2 monolayers (ML) on top of it (1 ML CoO=0.213 nm). It is clearly seen that the stepsterraces characteristics of the Fe(001)-$p(1 \times 1)$O surface are preserved after CoO deposition. We have actually observed this same behavior for all the CoO thicknesses explored, up to 7 ML. For larger thicknesses, the insulating character of the oxide did not allow to perform STM imaging. The observed morphology is strongly different from that reported for CoO ultra-thin films grown on noble metals, such as Ag [86]. In the latter case, it has been shown that the stepsterraces structure of the underlying substrate is clearly modified upon CoO deposition. In particular, vacancy islands form on the Ag(100) surface, and the removed Ag atoms form new protruding islands on the surface. Furthermore, the formation of Co oxide precursors has been reported in such cases. Previous XPS analysis suggested that this is not the case for the CoO/Fe interface, where the extra amount of oxygen leads to the formation of various Fe oxides, whose quantity depends on the growth temperature [92]. At the first stages of growth, namely below a nominal thickness of about 5 ML, the CoO layer is characterized by three-dimensional islands like those shown in Fig. 3.1b). Such islands are better seen in the 3030 nm^2 image reported

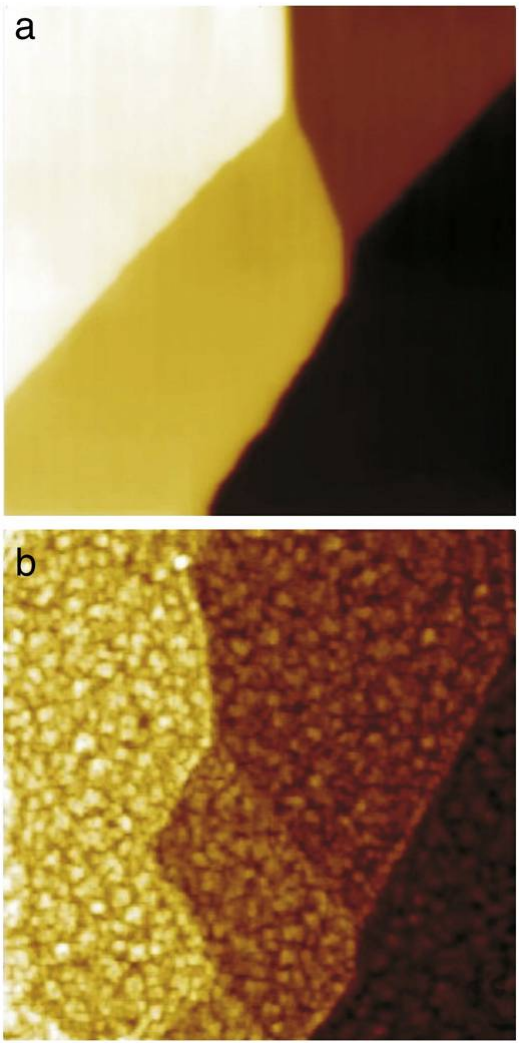

Figure 3.1: Room temperature 250×250 nm^2 STM images of: (a) the Fe(001)-$p(1 \times 1)$O surface (I=1 nA, V=1 V), and (b) the surface after the deposition of 2 ML CoO (I=1 nA, V=1 V).

in Fig. 3.2a). The latter refers again to a CoO film of nominal thickness 2 ML, grown on the Fe(001)-$p(1 \times 1)$O substrate. The maximum height of the islands, as measured by STM, is about 0.6 nm, which roughly corresponds to 3 nominal CoO ML, as it can be seen in the horizontal profile traced in Fig. 3.2(b). When increasing the nominal CoO thickness from 1 ML to less than 5 ML, the growth proceeds by an expansion of the lateral size of the islands. The relative number of islands, whose measured heights typically correspond to 2 or 3 nominal ML increases, as well. At this stage, the first full layer has not yet been completed. Such a conclusion can be drawn by

measuring the volume of the protruding islands after having set to zero the minimum height measured in the images. Such a volume corresponds in fact quite well with the expected amount of deposited CoO, as estimated from a calibrated thickness monitor (quartz microbalance). On the other hand, it is worth remarking that the topography, as measured by STM, can be strongly influenced by the surface electronic properties. It is therefore mandatory to be careful when comparing the nominal coverage, as estimated by the quartz microbalance, and the measured corrugation, as observed by STM.

The layer-plus-island growth begins at about 5 nominal ML. After such a threshold, in fact, the measured volume of the protruding islands is less than the total amount of oxide deposited. Only a fraction of the CoO layer is therefore represented by the observed islands. In particular, the measured height of the islands correspond typically to 2 or 3 nominal ML, and does not change even when increasing the CoO thickness, up to 7 ML.

This situation is represented by the 30×30 nm^2 image reported in Fig. 3.2(c), and by the relative horizontal profile traced in Fig. 3.2(d). Such an image refers to a CoO film of nominal thickness 5 ML. We underline that this finding is in good agreement with the results of previous LEED investigation, where it was reported that a diffraction pattern could only be observed for CoO films thicker than about 5 ML [92].

Our conclusions concerning the CoO growth sequence discussed above can be supported by a statistical analysis of some relevant parameters, as measured on the whole set of recorded STM images. In Fig. 3.3a) we report, as a function of the nominal CoO coverage, the evolution of the mean height of the three-dimensional islands, as measured in the STM images. It can be seen that such a parameter, after increasing in the first few steps of the CoO film growth, becomes roughly constant (with a value of about 0.4 nm, equivalent to about 2 nominal ML) up to 7 ML. This finding is well consistent with a layer plus- island growth regime. Fig. 3.3b) we report, again as a function of the nominal CoO coverage, the surface roughness of our samples, as measured by STM. The evolution of such a parameter is again well consistent with the transition from a pure three-dimensional morphology to a smoother layer-plus-island configuration.

A feature that deserves to be discussed, concerning the STM images of CoO ultra-thin films, is the rather poor lateral resolution. Such a feature was common to all the CoO thin films investigated, and did not depend on the measuring tip conditions, as several W tips have been employed with analogous results. It is worth emphasizing that all of our STM measurements have been performed at relatively low biases, i.e. equal to or below 1 V. Such a choice is due to the difficulty of realizing stable measurements sessions at higher biases. In the applied voltage range, different values of the

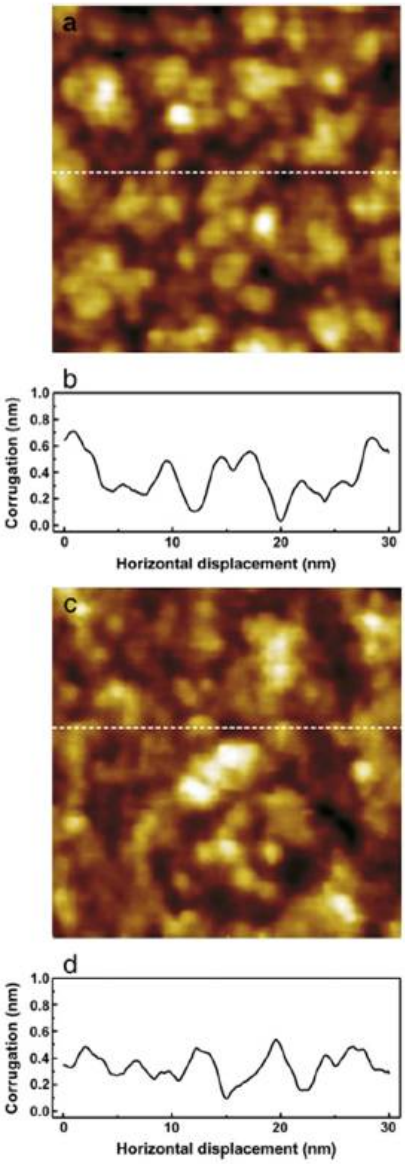

Figure 3.2: Panels (a) and (c) report 30×30 nm^2 STM images of 2 ML CoO on Fe(001) (I=1 nA, V=1 V) and 5 ML CoO on Fe(001) (I=0.5 nA, V=0.3 V), respectively. Panels (b) and (d) show the corrugation profiles along the dashed horizontal lines drawn on the images of panels (a) and (c), respectively.

bias, or even a change of sign, did not result in significantly different contrast in the STM images. It is known, when dealing with STM imaging of insulating materials, that the limited sample conductivity can be responsible of an intrinsic limitation on spatial resolution. The tunneling electron current I

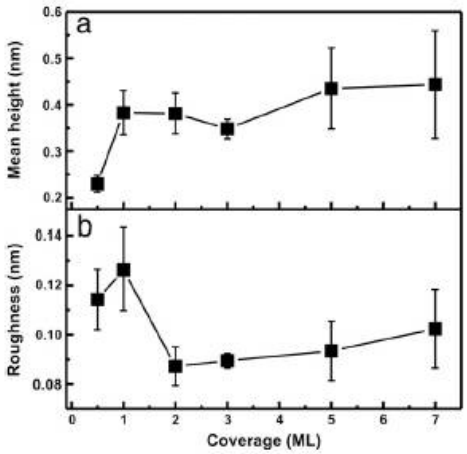

Figure 3.3: Panel (a) reports the mean height of the observed three-dimensional islands, as a function of CoO coverage. Panel (b) reports the surface roughness, as a function of CoO coverage.

flowing between tip and sample is typically obtained by integrating the tunneling probability, expressed as the combination of the available local density of states of the tip ρ_t and of the sample ρ_s , weighted by the transmission function of the vacuum barrier T, over the energy range determined by the sample bias V (here the E_F corresponds to V=0):

$$\int \rho_s(E)\rho_t(E - eV)T(z, E, V)dE; \tag{3.1}$$

where the function T depends on both the tip-sample distance z, the applied sample bias V and the average work function of the electrodes. Referring to such a description of the tunneling current, it should be required that either occupied or empty states of the sample are available for tunneling to or from the oxide and stabilize a tunneling current. For this reason, a large band gap around the E_F would hinder the tunnel process at low bias voltages. On the other hand, other mechanisms for tunneling can come into play and permit STM experiments at low biases, even on thick oxide films. Such mechanisms include, for instance, the increase of the oxide conductivity by the application of elevated temperatures or by doping, and the tunneling to a metal substrate through the oxide films [94]. In our case, the use of elevated temperatures, even though it has already demonstrated to be a successful approach in STM measurements of transition metal oxides such as CoO and NiO [93], does not represent a good choice, because of the very high chemical reactivity reported for CoO/Fe interfaces when increasing the sample temperature [92]. The mechanism of tunneling across the oxide films toward

the metal substrate seems actually more likely to be responsible for the tunneling current in our low-bias STM experiments on CoO thin films. Such a mechanism is based on the possible overlapping of the tip electronic states with the wave functions of the metal substrate, which must have sufficiently penetrated the oxide layer. For this reason, this mechanism is intrinsically limited to ultra-thin insulating films roughly less than a few nm thick. An estimate of the expected lateral resolution due to the low conductivity of the sample may be obtained by considering the extent of the space charge region that is formed below the tip. In fact, it is typically assumed that all of the voltage applied between sample and tip drops within the vacuum gap. In the case of low conductivity materials, on the contrary, it can be expected that the tip-sample bias can drop through such a space charge region, which extends across the sample surface [95]. Reasonably, the spatial extent of such a region, for very thin oxide films, must be of the order of the oxide thickness. As the tunneling actually occurs across the space charge region, the lateral resolution would be of the same order of its extent.

In a previous XPS investigation [92], it was evaluated that, at the very first stages of CoO growth, for a nominal thickness of about 1 ML, some iron oxides formed at the CoO/Fe interface, whose thickness was as high as twice the thickness of cobalt oxide. In that case, this corresponded to about 0.4 nm of iron oxides, to be added to the 0.2 nm height of the CoO layer, for a total oxide thickness of 0.6 nm. Such a value is in fairly good agreement with the experimental resolution of our STM images for such a low CoO coverage. Obviously we did not consider, in this analysis, other possible reasons for low lateral resolution in STM experiments, in particular the tip apex curvature. In the first place, we emphasize that the measurements have been repeatedly obtained with different W tips, and the images were characterized by a very similar spatial resolution. Secondly, we underline that we routinely obtained atomic resolution on several surfaces, including the oxidized Fe(001)-$p(1\times1)$O, with the same W tips, in analogous experimental conditions.

The above mentioned estimate for the total oxide thickness, being based on XPS measurements, could not give information on the spatial distribution of the oxide layer at the CoO/Fe interface.

We have investigated such an issue by taking STS data on different positions of the STM images, corresponding to either Fe substrate or CoO islands, for the case of very low coverages (about 0.5 ML) where such islands are more clearly distinguishable. Fig. 3.4(a) reports a 19×10 nm^2 STM image of such a surface, where different positions are labeled with capital letters. Position A refers to the Fe substrate, position B to an island of 1 ML height, position C to an island of 3 ML height (the latter kind of islands were only a

small fraction of the whole surface). Differential conductivity spectra have been collected at such positions, and are shown in Fig. 3.4 (b). Such curves have been rescaled and vertically translated for comparison purposes. It is clearly observed that the shape of the dI/dV spectra dramatically changes as a function of the measurement position. In particular, the curve taken at position A strongly resembles the known shape of the STS spectra of the Fe(001)-$p(1 \times 1)$O surface, being characterized by two peaks located about 0.5 eV below and 0.9 eV above the E_F, respectively, as shown in Ref. [31]. On the other hand, the spectra taken at positions B and C are characterized by the absence of peaks in a wide range around the E_F. These spectra thus probably refer to an insulator, as expected for CoO, whose optical gap is about 2.3 eV [86].

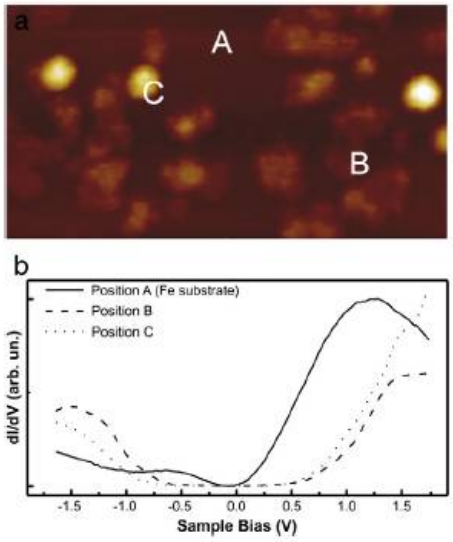

Figure 3.4: Panel (a) reports a 19×10 nm^2 STM images of 0.5 ML CoO on Fe(001)-$p(1 \times 1)$O (I=1 nA, V=1 V). The capital letters refer to: A the Fe substrate, B a CoO island of 1ML height, C a CoO island of 3 ML height. Panel (b) reports dI/dV curves relative to: position A (continuous line), position B (dashed line) and position C (dotted line).

Such measurements have been repeatedly recorded on several different positions on the surface, with very similar results. We can thus infer that the iron oxides forming at the CoO/Fe interface during the first stages of growth preferentially develop below the CoO islands, i.e. in presence of the real interface. Our observations suggest that the chemical reactions occurring at the interface are strongly driven by the proximity between Co and Fe atoms, which very likely promotes the dissociation of molecular oxygen.

Oxygen in the atomic form is in fact much more mobile and reactive, as thoroughly discussed in the case of the NiO/Fe interface produced by the reactive deposition technique, and would thus induce a strong oxidation of the Fe atoms close to the interface, despite the surface itself had previously been passivated by oxygen adsorption.

On the other hand, our measurements emphasize the noticeable stability of the Fe(001)-$p(1\times1)$O surface alone with respect to further oxidations, thus confirming the good choice of such a surface as a substrate for the realization of AFM/FM layered systems comprising transition metal oxides.

Once the growth mode of CoO/Fe interfaces has been investigated, we have realized Fe/CoO/Fe trilayers. Fig. 3.5 (a) reports the surface morphology of a trilayer characterized by a 10 ML thick CoO spacer and by a Fe upper layer about 1.5 nm thick. The 150×150 nm^2 STM image shows, in particular, evidence of the original terraces of the underlying substrate. On a smaller scale, as reported in the 30×30 nm^2 STM image of Fig. 3.5(b), one can observe islands similar to those present on the CoO/Fe interface. Such islands, as evidenced by the horizontal profile traced in Fig. 3.5(c), have typical heights of 0.3 0.4 nm (equal to about 23 iron atomic layers), and typical widths of the order of 10 nm.

One interesting feature of our Fe/CoO/Fe trilayers, which has been previously pointed out and discussed [96], is the occurrence of very small magnetic domains on the Fe top layer, with in-plane direction of the magnetization. Such a phenomenology has been interpreted, also considering several similar findings reported for the Fe/NiO/Fe case [79], on the basis of the role that the exchange interaction at the FM/ AFM interfaces plays, with respect to the stabilization of very small domains. The magnetic domains structure in FM films would usually be determined by the balance between magneto-crystalline anisotropy and exchange energy, and the typical sizes of the magnetic domains extend over several micrometers or even more. At variance with this scenario, in the case of Fe/CoO/Fe and Fe/NiO/Fe systems such sizes, as observed by spin-polarized low-energy electron microscopy and photo-electron emission microscopy, were as low as few tens of nanometers.

Micromagnetic models have been invoked and implemented in order to explain the experimental observations [79]. In particular, the fundamental role of magnetic defects (uncompensated moments) at the interfaces has been thoroughly discussed. The results reported in the present thesis offer the possibility of examining the role that the morphology of the system plays in determining the micromagnetic structure. In particular, as discussed in previous publications [97], the significant length scales with respect to the domain sizes are such that there exists a magnetic roughness due to variations in the AFM thickness at the AFM/FM interfaces. If the induced magnetic

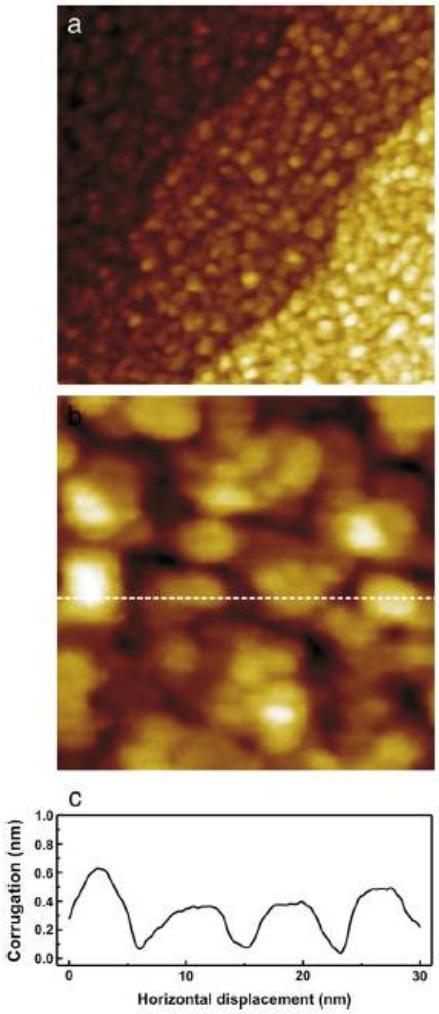

Figure 3.5: Panel (a) reports a 150×150 nm^2 STM images of a 1.5 nm Fe/10 ML CoO/Fe(001) trilayer (I=1 nA, V=1 V). Panel (b) reports a 30×30 nm^2 blow-up of the image shown in panel (a) (I=0.5 nA, V=0.2 V). Panel (c) shows the corrugation profile along the dashed horizontal line drawn on the image of panel (b).

defect moments do not cancel with each other on a length scale of the order of at least the minimum size of the observed domains, the latter can therefore be stabilized [79]. The present measurements show that the islands observed on top of our Fe/CoO/Fe structures are in general smaller than the magnetic domains, whose minimum sizes were reported to be as small as about 30 nm in radius [92]. On the other hand, it is clear that the topography of our trilayer structure can be the source of the magnetic roughness previously

mentioned. Future magnetic measurements, such as spin-polarized STM, could help in disentangling the actual distribution of the magnetic domains as a function of the spatial position.

In summary, in this section we have investigated the morphology of CoO ultrathin films grown on Fe(001) and of Fe/CoO/Fe layered structures on the nanometer scale by means of STM. We observed three dimensional CoO islands in the first stages of the CoO/Fe interface formation, up to about 5 nominal atomic layers, then turning to layer plus- island growth for higher thicknesses. By collecting STS on different positions of the CoO/Fe interface with very low coverage, we concluded that the previously observed chemical interactions at such an interface occur mostly below the CoO islands, thus emphasizing the role of the CoFe proximity in determining the reaction mechanisms. The surface morphology of the Fe/CoO/Fe trilayers preserves both the structure of the developed CoO/Fe interface and that of the underlying Fe layer. We have discussed the implications of these observations on the known magnetic domains structure of the upper Fe layer.

3.3 Cobalt oxide nanowires

In this section are presented some preliminary results about the cobalt oxide nanowires grown on the P(1 1 19) surface. The Pd(1 1 19) is a surface vicinal of Pd(001), in which the nominal terrace width is ten atoms and the steps are running along the [110] direction. Clean Pd(1 1 19) surfaces were prepared by 1.5 keV Ar+ ion sputtering, followed by annealing to 1000 K for several minutes, and by heating cycles in O_2 atmosphere (2×10^{-7} mbar) at 570 K followed by a final short flash to 1000 K in UHV. Exposing the clean Pd (1 1 19) surface to an oxygen pressure of 1×10^{-8} mbar at 570 K and subsequent cooling in oxygen atmosphere resulted in a well ordered chemisorbed $p(2 \times 2)-O$ layer (see Fig. 3.6).

The Co deposition was made on the $p(2 \times 2)$-O surface by molecular beam epitaxy. The best kinetic conditions to obtain uniformly decorated steps were found to be reactive deposition in 1×10^{-8} mbar oxygen atmosphere with the sample kept at room temperature and subsequent post annealing at 570 K for 3 minutes. The STM images and spectroscopic curves were acquired both at room temperature and at low temperature (4 K) by a commercial available Createc STM.

Figure Fig. 3.7 displays the LEED pattern and the topography of the vicinal surface decorated with cobalt oxide nanowires. In the LEED pattern in addition to the $p(2 \times 2)-O$ spots we find that an additional spot splitting occurs along the {110} reciprocal space direction . These spots can be related

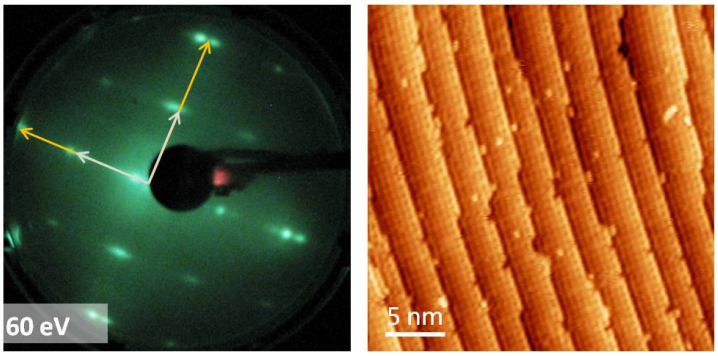

Figure 3.6: LEED pattern at 60 eV (left side) and STM topography (right side) of the Pd(1 1 19)$p(2 \times 2)-$O surface.

to a long range periodicity along the steps direction, well visible also in the STM image shown in Fig. 3.7. A closer inspection of the STM images shows that this periodicity is given by the presence of kinks protruding from the steps, as statistically analyzed in Fig. 3.7 (d).

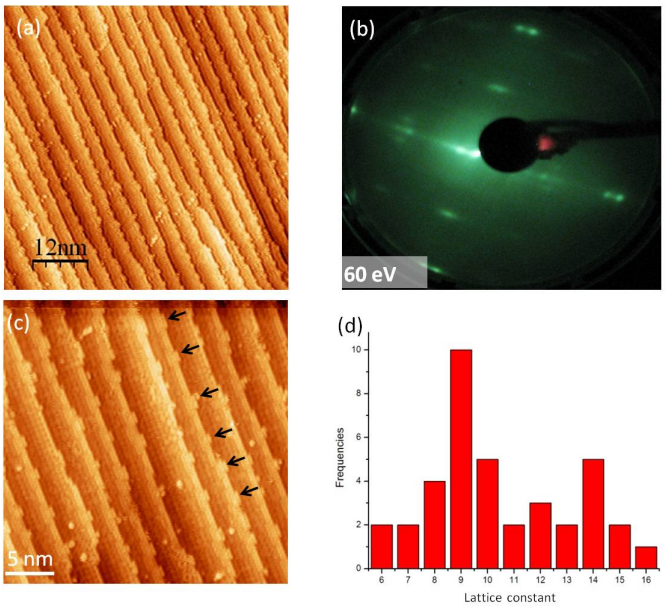

Figure 3.7: Cobalt oxide nanowires: Panels (a) and (c): topographic image of the decorated steps. The arrows in (c) correspond to the kink positions. Panel (b) LEED pattern at 60 eV. An additional spot splitting perpendicular to the spot splitting due to the step distribution is visible. Panel (d) statistical distribution of the kink-kink separation. The most likely kink-kink distance is 9 atomic Pd lattice constant.

In Fig. 3.8 there is a detail of the step decoration, in which the lines following the step edge are drawn. The decorated steps have an irregular shape, whereas the steps of the surface before the evaporation are much more straight. This may indicate that during the decoration process some Pd atoms belonging to the step are displaced and replaced by cobalt atoms.

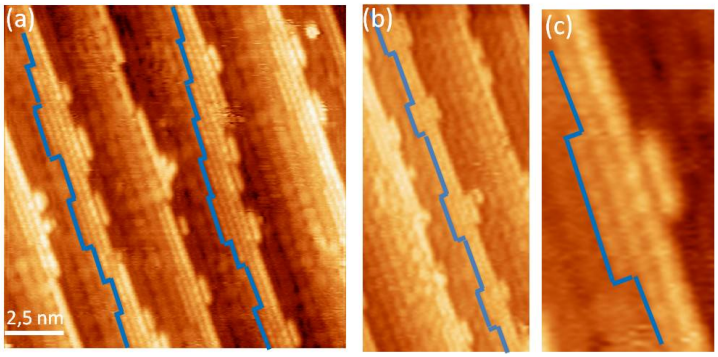

Figure 3.8: STM topography of the kink structure.

The basic structure of the decorated steps is presented in the zoom images in Fig. 3.8 (b) and (c), in which there is a double row of bright spots running along the step edge and the "kink" structure. Corresponding to every protruding kink the step decoration is composed by three rows of bright spots. An important issue that has to be discussed in order to establish the nanowires atomistic structure is the nature of the bright spots forming the double row decorating the steps. For cobalt oxide nanolayers wetting the Pd(001) surface two different phases have been reported, namely the (9×2) and the (4×2) [101]. In these two structures the oxygen atoms are imaged respectively as bright and dark spots, so it is not trivial to establish if in the case of the quasi one dimensional structure we are imaging the oxygen or the cobalt atoms.

When the cobalt coverage on Pd(1 1 19) is increased up to 1 equivalent ML the step structure is completely lost, the surface undergoes step bunching and is covered by the CoO (9×2) phase (see Fig. 3.9). The CoO (9×2) wetting layer has already been observed on the flat Pd(001), when the cobalt oxide is obtained at low oxygen chemical potential [101]. In this case the wetting layer of cobalt oxide causes an instability in the morphology of the vicinal surface, inducing a strong step bunching. The situation is completely different from the stabilization of the step structure induced by the wetting layer of manganese oxide grown on the vicinal surfaces of Pd(001) [103].

In Fig. 3.10 the STS spectra taken on the middle of the terrace and on the top of the cobalt oxide nanowire are shown. An interesting feature is that it is

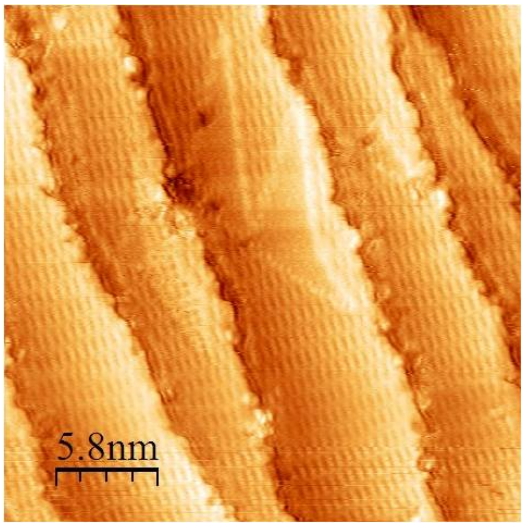

Figure 3.9: STM topography of the surface after the reactive deposition of 1 equivalent monolayer of cobalt in O_2 pressure (1×10^{-8} mbar).

present a peak located at about -200 meV below the E_F in both spectra, but the intensity on the nanowire is much larger. One possible interpretation is that the enhanced intensity measured is due to a charge transfer from the Pd terrace to the oxide nanowire. Charge transfer perpendicular to the surface between an oxide overlayer and a metallic substrate is a well known phenomenon that can modify the sample work function [75]. In our case the charge may flow from the terrace to the decorated step, giving rise to the observed enhancement of the surface state intensity.

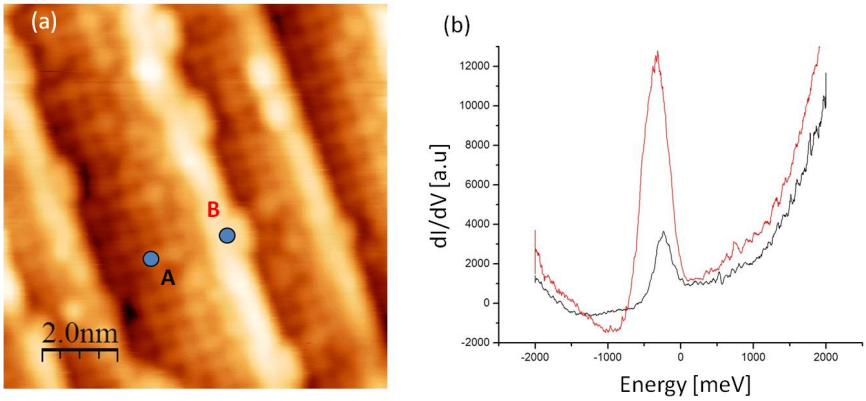

Figure 3.10: STS spectra measured on the Pd(001)-$p(2 \times 2)$O (a) and on the step decorated with cobalt oxide (b) (measurement set-point: current $I_t = 1$ nA, bias $V_b = 1$ V)

In Fig. 3.11 are shown the field emission resonances spectra (FERs) taken across a line crossing the Pd(001)-$p(2 \times 2)$O region and the decorated steps. In the curves measured on the top of the $p(2 \times 2)$ region there is a peak located at 3.6 eV and the first resonance at 6.6 eV, while in the nanowires region there is a peak at 4.7 eV and the first resonance is at 7.2 eV. As the FERs start to appear for voltages around the sample work function [102], this shift toward higher energy may indicate that the decoration increases the local work function with respect to the Pd(001) terrace.

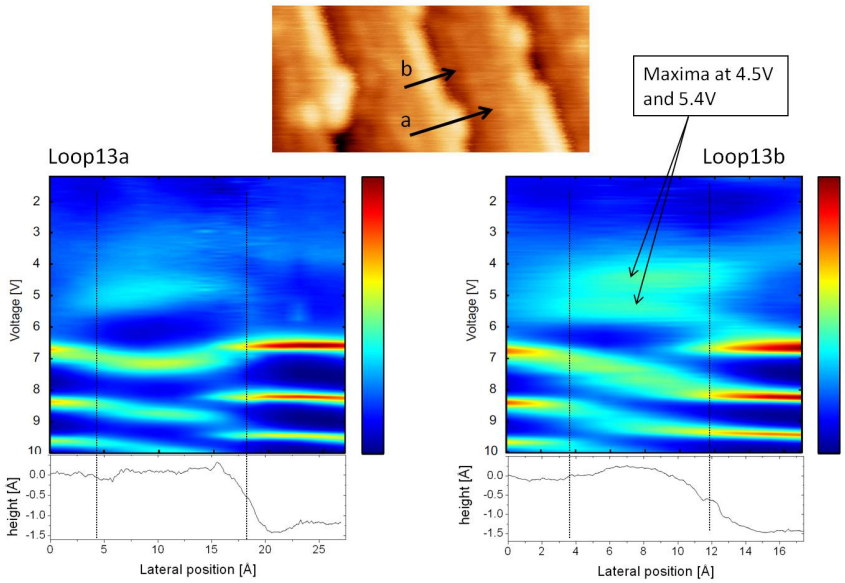

Figure 3.11: Field emission resonances spectra (FERs) taken across a line crossing the Pd(001)-$p(2 \times 2)$O region and on the top of the decorated steps.

In conclusion, in this section we have shown that quasi one dimensional structures of cobalt oxide can be obtained by means of step decoration of the Pd(1 1 19) surface. This procedure leads to a periodic kinked structure of the steps, with a periodicity corresponding to 9 atomic lattice constant of Pd. The electronic structure of the surface is dominated by a surface state located 200 meV below the E_F. This state is present both on the Pd(001) terraces and in the cobalt oxide nanowire, with a remarkable difference in the intensity. Further experimental and theoretical investigations are needed to disentangle the atomic structure of the nanowires and the observed intensity difference observed in the surface state.

Bibliography

[1] J.Barth, G.Costantini, K.Kern Nature **437**, 671 (2005).

[2] Gates,B.D. Chem. Rev. **105**, 1171 (2005).

[3] For a review about crystal surfaces in and out of equilibrium see, for instance, C. Misbah and O. Pierre-Louis, Rev. Mod. Phys. **82**, 981 (2010).

[4] R. Bertacco and F. Ciccacci, Phys. Rev. B **59**, 4207 (1999).

[5] F. Bisio, R. Moroni, M. Canepa, L. Mattera, R. Bertacco, F. Ciccacci, Phys. Rev. Lett. **83**, 4868 (1999).

[6] P. Bonanno, M. Canepa, P. Cantini, R. Moroni, L. Mattera, S. Terreni, Surf. Sci. **697**, 454 (2000).

[7] R. Moroni, F. Bisio, A. Gussoni, M. Canepa, L. Mattera, Surf. Sci. **850**, 482 (2001).

[8] G. A. Somorjai, Introduction to Surface Chemistry and Catalysis (Wiley, New York, 1994).

[9] S. S. Parihar, H. L. Meyerheim, K. Mohseni, S. Ostanin, A. Ernst, N. Jedrecy, R. Felici, and J. Kirschner, Phys. Rev.B **81**, 075428 (2010).

[10] S. R. Chubb and W. E. Pickett, Phys. Rev. Lett. **58**, 1248 (1987).

[11] K. O. Legg, F. Jona, D. W. Jepsen, and P. M. Marcus, Phys. Rev. B **16**, 5271 (1977).

[12] P. Blonski, A. Kiejna, and J. Hafner, Surf. Sci. **590**, 88 (2005).

[13] P. Blonski, A. Kiejna , and J. Hafner, J. Phys.: Condens. Matter **19**, 096011 (2007).

[14] G. Ehrlich and F. G. Hudda, J. Chem. Phys. **44**, 1039 (1957).

[15] R. L. Schwoebel, J. Appl. Phys. **40**, 614 (1969).

[16] R. L. Schwoebel and E. J. Shipley, J. Appl. Phys. **37**, 3682 (1966).

[17] Z. Zhang, M. G. Lagally, Phys. Rev. Lett. **72**, 693 (1994).

[18] A. Latyshev, A. Aseey, A. Krasilnikov, and S. Stenin, Surf. Sci. **213**, 157 (1989).

[19] C. Duport, P. Nozi'eres, and J. Villain, Phys. Rev. Lett. **74**, 134 (1995).

[20] S. Paulin, F. Gillet, O. Pierre-Louis, and C.Misbah, Phys. Rev. Lett. **86**, 5538 (2001).

[21] P. Muller and A. Saul, Surface Science Reports **54**, 157 (2004).

[22] J. Tersoff, Y. H. Phang, Z. Zhang, and M. G. Lagally, Phys. Rev. Lett. **75**, 2730 (1995).

[23] H. Ibach, Physics of Surfaces and Interfaces (Springer, Berlin, 2006), p.144

[24] H. Hibach, Surf. Sci. Rep. **29**, 193 (1997).

[25] M. M. J. Bischoff, T. K. Yamada, C. M. Fang,* R. A. de Groot, and H. van Kempen, Phys. Rev. B **68**, 045422 (2003).

[26] J. P. Perdew, K. Burke, and M. Ernzerhof, Phys. Rev. Lett. **77**, 3865 (1996).

[27] D. Vanderbilt, Phys. Rev. B **41**, 7892 (1990).

[28] P. Giannozzi, S. Baroni, N. Bonini, M. Calandra, R. Car, C. Cavazzoni, D. Ceresoli, G. L. Chiarotti, M. Cococcioni, I. Dabo et al., J. Phys.: Condens. Matter **21**, 395502 (2009); http:// www.quantum-espresso.org

[29] A. Selloni, P. Carnevali, E. Tosatti, and C. D. Chen, Phys. Rev. B **31**, 2602 (1985).

[30] N. D. Lang, Phys. Rev. B **34**, 5947 (1986).

[31] F. Donati, P. Sessi, S. Achilli, A. Li Bassi, M. Passoni, C. S. Casari, C. E. Bottani, A. Brambilla, A. Picone, M. Finazzi, L. Duò, M. I. Trioni, and F. Ciccacci, Phys. Rev. B **79**, 195430 (2009).

[32] P.-O. Lwdin, J. Chem. Phys. **38**, 365 (1950).

[33] H. Ishida, Phys. Rev. B **63**, 165409 (2001).

[34] J. E. Inglesfield, J. Phys. C **14**, 3795 (1981).

[35] J. A. Stroscio, D. T. Pierce, A. Davies, R. J. Celotta, and M. Weinert, Phys. Rev. Lett. **75**, 2960 (1995).

[36] V. A. Ukraintsev, Phys. Rev. B **53**, 11176 (1996).

[37] J. A. Stroscio, R. M. Feenstra, and A. P. Fein, Phys. Rev. Lett. **58**, 1668 (1987)

[38] M. Passoni, F. Donati, A. Li Bassi, C. S. Casari, and C. E. Bottani, Phys. Rev. B **79**, 045404 (2009).

[39] A. Li Bassi et al., Appl. Phys. Lett. **91**, 173120 (2007).

[40] E. Yu. Tsymbal, I. I. Oleinik, and D. G. Pettifor, J. Appl. Phys. **87**, 5230 (2000).

[41] C. M. Fang, R. A. de Groot, M. M. J. Bischoff, and H. van Kempen, Surf. Sci. **445**, 123 (2000)

[42] A. Clarke, N. B. Brookes, P. D. Johnson, M. Weinert, B. Sinkovi, and N. V. Smith, Phys. Rev. B **41**, 9659 (1990).

[43] R. M. Feenstra, G. Meyer, and K.-H. Rieder, Phys. Rev. B **69**, 081309(R) (2004)

[44] L. Limot, T. Maroutian, P. Johansson, and R. Berndt, Phys. Rev. Lett. **91**, 196801 (2003).

[45] W. A. Hofer, J. Redinger, A. Biedermann, and P. Varga, Surf. Sci. **482-485**, 1113 (2001).

[46] J. Mysliveek, A. Strecka, J. Steffl, P. Sobotk, I. Otdal, and B. Voigtlnder, Phys. Rev. B **73**, 161302(R) (2006).

[47] S. De Rossi, L. Duò, and F. Ciccacci, Europhys. Lett. **32**, 687 (1995).

[48] L. Braicovich, F. Ciccacci, E. Puppin, A. Svane, and O. Gunnarsson, Phys. Rev. B **46**, 12165 (1992)

[49] J. A. Stroscio, D. T. Pierce, and R. A. Dragoset, Phys. Rev. Lett. **70**, 3615 (1993).

[50] J. A. Stroscio, D. T. Pierce, M. D. Stiles, A. Zangwill, and L. M. Sanders, Phys. Rev. Lett. **75**, 4246 (1995).

[51] M. Nyvlt, F. Bisio, J. Franta, C. L. Gao, H. Petek, and J. Kirschener Phys. Rev. Lett. **95**, 127201 (2005).

[52] J. Camarero, J. Ferrón, V. Cros, L. Gómez, A. L. Vázquez de Parga, J. M. Gallego, J. E. Prieto, J. J. de Miguel, and R. Miranda Phys. Rev. Lett. **81**, 850 (1998).

[53] J. Vrijmoeth, H. A. Van Der Vegt, J. A. Meyer, E. Vlieg, and R. J. Behm, Phys. Rev. Lett. **72**, 3843 (1994).

[54] S.Esch, M. Hohage, T. Michely, and G. Comsa, Phys. Rev. Lett. **72**, 518 (1994).

[55] G. Leonardelli, E. Lundgren, and M. Schmid, Surf. Sci. **490**, 29 (2001).

[56] K. Bromann, H. Brune, H. Roder, and K. Kern, Phys. Rev. Lett. **75**, 677 (1995).

[57] H. Roder, K. Bromann, H. Brune, and K. Kern, Surf. Sci. **376**, 13 (1997).

[58] J. J. de Miguel and R Miranda, J. Phys.: Condens. Matter **14** R1063R1097 (2002)

[59] J. Unguris, R.J. Celotta, D.T. Pierce, Phys. Rev. Lett. **67** (1991) 140.

[60] J. Unguris, R.J. Celotta, D.T. Pierce, Phys. Rev. Lett. **69** (1992) 1125.

[61] A. Davies, J.A. Stroscio, D.T. Pierce, R.J. Celotta, Phys. Rev. Lett. **76** (1996) 4175.

[62] A. Davies, J.A. Stroscio, D. Pierce, J. Unguris, R. Celotta, J. Magn. Magn. Mater. **165** 82 (1997.

[63] J. Bland, B. Heinrich (Eds.), Ultrathin Magnetic Structures Vols I and II, Springer, 1994.

[64] H.L. Meyerheim, D. Sander, R. Popescu, W. Pan, I. Popa, J. Kirschner, Phys. Rev. Lett. **99** 116101 (2007).

[65] R.-F. Xiao, J.I.D. Alexander, F. Rosenberger, Phys. Rev. A **43** 2977 (1991).

[66] M. Schmid, G. Leonardelli, M. Sporn, E. Platzgummer, W. Hebenstreit, M. Pinczolits, and P. Varga Phys. Rev. Lett. **82** 355 (1999).

[67] A. Picone, A. Brambilla, A. Calloni, L. Du'o, M. Finazzi, and F. Ciccacci Phys. Rev. B **83**, 1235402 (2011).

[68] A. Calloni, A. Picone, A. Brambilla , M. Finazzi, L. Duò, F. Ciccacci Surf. Sci. **605**, 20922096 (2011).

[69] B. Heinrich, Z. Celinski, J. F. Cochran, W. B. Muir, J. Rudd, Q. M. Zhong, A. S. Arrott, K. Myrtle, and J. Kirschner, Phys. Rev. Lett. **64**, 673 (1990).

[70] Z. Q. Wang, Y. S. Li, F. Jona, and P. M. Marcus, Solid State Commun. **61**, 623 (1987).

[71] A. V. Mijiritskii, P. J. M. Smulders, V. Ya. Chumanov, O. C. Rogojanu, M. A. James, and D. O. Boerma Phys. Rev. B **58**, 8960 (1998).

[72] C. S. Tian, D. Qian, D. Wu, R.H. He, Y. Z. Wu, W.X. Tang, L. F. Yin, Y. S. Shi, G. S. Dong, and X. F. Jin, X. M. Jiang, F. Q. Liu, H. J. Qian, K. Sun, L. M. Wang, G. Rossi, Z. Q. Qiu, and J. Shi Phys. Rev. Lett. **94**, 137210 (2005).

[73] V. L. Moruzzi et al., Phys. Rev. Lett. **57**, 2211 (1986); Phys. Rev. B **34**, 1784 (1986);

[74] A. Picone, G. Fratesi, A. Brambilla, P. Sessi, F. Donati, S. Achilli, L. Maini, M. I. Trioni, C. S. Casari, M. Passoni, A. Li Bassi, M. Finazzi, L. Duò, and F. Ciccacci1 Phys. Rev. B **81**, 115450 (2010).

[75] Netzer, F. P.; Allegretti, F.; Surnev, S. Low-dimensional oxide nanostructures on metals: Hybrid systems with novel properties. J. Vac. Sci. Technol. B **28**, 3268503 (2010)

[76] G. Pacchioni and S. Valeri, Oxide Ultrathin Films (WILEY-VCH, Germany, 2012)

[77] G. Ertl, H. Kntzinger, F. Schueth, J. Weitkamp (Eds.), Handbook of Heterogeneous Catalysis, second ed., Wiley-VCH, Weinheim, 2008.

[78] See, for instance S.D. Bader, J.L. Erskine, in: B. Heinrich, J.A.C. Bland (Eds.), Ultrathin Magnetic Structures, Springer Verlag, Berlin, 1994.

[79] M. Finazzi, L. Duò, F. Ciccacci, Surf. Sci. Rep. **64** (4) 139 (2009).

[80] W.H. Meiklejohn, C.P. Bean, Phys. Rev. **102** 1413 (1956).

[81] J. Nogus, I.K. Schuller, J. Magn. Magn. Mater. **192** 203 (1999).

[82] T.J. Regan, H. Ohldag, C. Stamm, F. Nolting, J. Lning, J. Sthr, R.L. White, Phys. Rev. B **64** 214422 (1998).

[83] J. Wu, J.S. Park, W. Kim, E. Arenholz, M. Liberati, A. Scholl, Y.Z. Wu, C. Hwang, Z.Q. Qiu, Phys. Rev. Lett. **104** 217204.(1998).

[84] S.I. Csiszar, M.W. Haverkort, Z. Hu, A. Tanaka, H.H. Hsieh, H.-J. Lin, C.T. Chen, T. Hibma, L.H. Tjeng, Phys. Rev. Lett. **95** (2005) 187205.

[85] C. Fleischmann, F. Almeida, J. Demeter, K. Paredis, A. Teichert, R. Steitz, S. Brems, B. Opperdoes, C.V. Haesendonck, A. Vantomme, K. Temst, J. Appl. Phys. **107** 113907 (2010).

[86] R. Shantyr, C. Hagendorf, H. Neddermeyer, Surf. Sci. **566568** 68 (2004).

[87] I. Sebastian, M. Heiler, K. Meinel, H. Neddermeyer, Appl. Phys. A **66** S525 (1998).

[88] C. Giovanardi, L. Hammer, K. Heinz, Phys. Rev. B **74** 125429 (2006).

[89] P. Luches, V. Bellini, S. Colonna, L. Di Giustino, F. Manghi, S. Valeri, and F. Boscherini Phys. Rev. Lett. **96** 106106 (2006).

[90] P. Torelli, E.A. Soares, G. Renaud, L. Gragnaniello, S. Valeri, X.X. Guo, P. Luches, Phys. Rev. B **77** 081409 (2008).

[91] F. Allegretti, G. Parteder, M. Ramsey, S. Surnev, F. Netzer, Surf. Sci. **601** L73 (2007).

[92] A. Brambilla, P. Sessi, M. Cantoni, L. Duò, M. Finazzi, F. Ciccacci, Thin Solid Films **516** 7519 (2008).

[93] M.R. Castell, S.L. Dudarev, G.A.D. Briggs, A.P. Sutton, Phys. Rev. B **59** 7342 (1999).

[94] N. Nilius, Surf. Sci. Rep. **64** 595 (2009).

[95] D.A. Bonnell, Prog. Surf. Sci. **57** 187 (1998).

[96] A. Brambilla, P. Sessi, M. Cantoni, M. Finazzi, N. Rougemaille, R. Belkhou, P. Vavassori, L. Duò, F. Ciccacci, Phys. Rev. B **79** 172401 (2009).

[97] L. Duò, M. Finazzi, F. Ciccacci (Eds.), Magnetic Properties of Antiferromagnetic Oxide Materials, Wiley-VCH, 2010.

[98] B. Voigtlander, G. Meyer, and N.M. Amer, Phys. Rev. B **44**, 10 354 (1991).

[99] J. de la Figuera, J.E. Prieto, C. Ocal, and R. Miranda, Phys. Rev. B **47**, 13 043 (1993)

[100] Zhang, Q. Niu, and C. Shih, Phys. Rev. Lett. **80**, 5381 (1998).

[101] L. Gragnaniello, S. Agnoli, G. Parteder, A. Barolo, F. Bondino, F. Allegretti, S. Surnev, G. Granozzi, and F. P. Netzer, Surf. Sci. **604**, 2002 (2010).

[102] K. H. Gundlach, Solid-State Electron. **9**, 949 (1966).

[103] Fanghua Li, Francesco Allegretti, Svetlozar Surnev, Falko P. Netzer Surf. Sci. Lett. **604**, L43 2010

List of pubblication

Scanning tunneling spectroscopy of the Fe(001)-p(1x1)O surface Physical Review B **79**, 195430 (2009)

Atomic corrugation in scanning tunneling microscopy images of the Fe(001)-$p(1 \times 1)$O surface Physical Review B **81**, 115450 (2010)

Scanning tunneling microscopy investigation of CoO/Fe(001) and Fe/CoO/Fe(001) layered structures Surface Science **605**, 95-100 (2011)

Effects of temperature on the oxygen aided Cr growth on Fe(001) Surface Science **605**, 2092-2096 (2011)

Oxygen-induced effects on the morphology of the Fe(001) surface in out-of-equilibrium conditions Physical Review B **81**, 235402 (2011)